aerospace

MDPI

*Article*

# Preliminary Sizing of the Electrical Motor and Housing of Electromechanical Actuators Applied on the Primary Flight Control System of Unmanned Helicopters

**Jeremy Roussel [1,2,*], Marc Budinger [1] and Laurent Ruet [2]**

[1] National Institute of Applied Sciences of Toulouse (INSA), Clement Ader's Institute (ICA), 31077 Toulouse, France
[2] Airbus Helicopters, 13700 Marignane, France
* Correspondence: jroussel@insa-toulouse.fr

**Abstract:** Helicopter dronization is expanding, for example, the VSR700 project. This leads to the integration of electromechanical actuators (EMAs) into the primary flight control system (PFCS). The PFCS is in charge of controlling the helicopter flight over its four axes (roll, pitch, yaw, and vertical). It controls the blade pitch thanks to mechanical kinematics and actuators. For more than 60 years, the actuators have been conventionally using the hydraulic technology. The EMA technology introduction involves the reconsideration of the design practices. Indeed, an EMA is multidisciplinary. Each of its components introduces new design drivers and new inherent technological imperfections (friction, inertia, and losses). This paper presents a methodology to specify and pre-design critical EMAs. The description will be focused on two components: the electrical motor and the housing. This includes a data-driven specification, scaling laws for motor losses estimation, and surrogate modeling for the housing vibratory sizing. The tools are finally applied to two study cases. The first case considers two potential redundant topologies of actuation. The housing sizing shows that one prevails on the other. The second case considers the actuators of helicopter rotors. The electrical motor sizing highlights the importance of designing two separate actuators.

**Keywords:** specification; flight analysis; dimensional analysis; vibration; multidisciplinary optimization



**Citation:** Roussel, J.; Budinger, M.; Ruet, L. Preliminary Sizing of the Electrical Motor and Housing of Electromechanical Actuators Applied on the Primary Flight Control System of Unmanned Helicopters. *Aerospace* **2022**, *9*, 473. https://doi.org/10.3390/aerospace9090473

Academic Editor: Gianpietro Di Rito

Received: 30 June 2022
Accepted: 19 August 2022
Published: 25 August 2022



## 1. Introduction

### *1.1. Context*

#### 1.1.1. Helicopter Dronization

Today, we observe a fast increase in the number of projects about OPVs (Optional Pilot vehicles), UASs (Unmanned Aerial Systems), UAVs (Unmanned Aerial Vehicles), UAM (Urban Air Mobility), and VTOL (Vertical Take-Off Landing). For instance, the Ehang 184, the Vahana, the CityAirbus, and Boeing's self-piloted passenger drone can be seen on the civil range; the aerial fighter Northrop Grumman X-47B, the Airbus VSR700 (Figure 1), and the Leonardo AWHero can be seen on the military range. Furthermore, the market for aerial delivery already grows, with vehicles carrying parcels weighing less than 10 kg (DPD France drones in rural areas) up to 100 kg (Kawasaki K-Racer X1 drone prototype). It is clear that flying vehicles and future ones are already required to develop new functionalities to be more autonomous and to be safer. Reducing pilots' working load is part of the current helicopter development roadmaps for enhanced safety. Thus, today's market trend is globally facing a technological watershed toward more electrical solutions. Aircraft makers aim for the More Electric Aircraft (MEA) achievement [1]. The drone concept comes progressively by the implementation of new electrical solutions on already existing vehicles [2].


**Figure 1.** VSR700, the multi-mission naval UAS (©Airbus).

1.1.2. Primary Flight Control Systems: From Hydraulic to Electromechanical Technologies

The primary flight control system (PFCS) is in charge of controlling the helicopter flight over its four axes (roll, pitch, yaw, and vertical) by the control of the blade attack angles. The paper [3] describes the PFCS with pictures. More details can be found in the book [4] and the handbook [5]. The automatic pilot function is ensured through EMAs located in series and in parallel with the mechanical kinematic (Figure 2a).

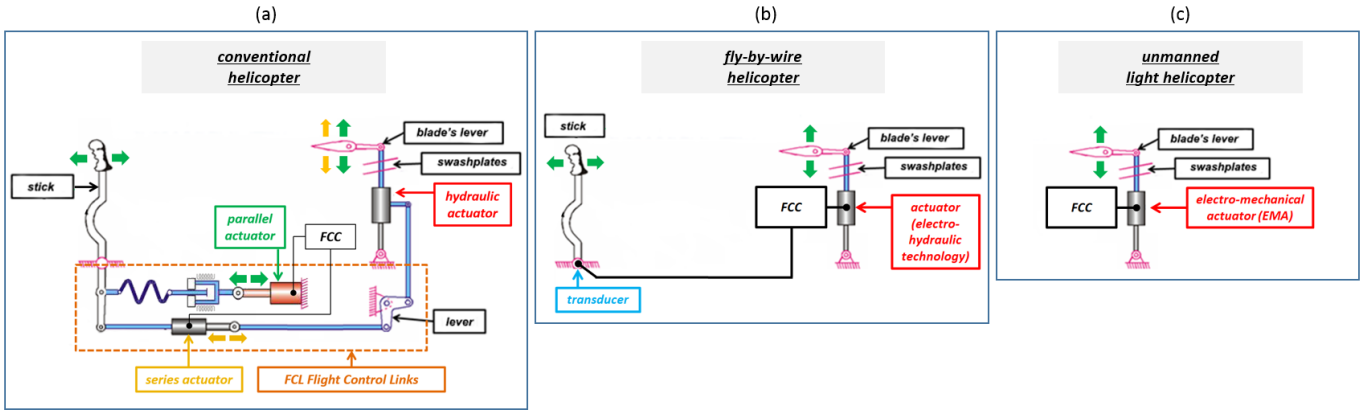


**Figure 2.** PFCS architectures: sketch of principle. From (**a**–**c**), this figure shows basically the evolution of PFCS architectures as it applies to autonomous helicopters. This evolution clearly shows that the helicopter mass can be significantly reduced with the reduction in part numbers. As long as the actuation control loop is concerned, this part number reduction decreases the response delay sources. The quid pro quo for it is the increase in the actuator critical level because it gathers nearly all piloting functions.

Only one helicopter in the Airbus fleet (NH90) is fly-by-wire. The hydraulic actuators (Direct Drive Valve, DDV) are commanded directly by four electrical torque-motors connected to the FCC (Flight Control Computer), as shown in Figure 2b.

The hydraulic technology has been conventionally used in actuators for more than 60 years [1,6]. A new trend uses EMAs as substitutes for hydraulic actuators in the PFCS in actual helicopters or as part of fly-by-wire PFCSs in new autonomous helicopters (Figure 2c). This requires the reconsideration of the design practices right at the preliminary design phase. The VSR700 (Figure 1) is a use case. It is an already proved light helicopter (Cabri G2) turned into a drone by the integration of electrical components. These components include four EMAs in the PFCS.

1.1.3. Business Need

Today's business need is to perform EMA preliminary studies and learn more about this technology. Indeed, further to an application in the primary flight control system (main rotor and tail rotor), the EMA technology finds interest in many other helicopter applications, such as the automatic pilot actuators or the secondary flight control system

(SFCS). This includes the actuation of landing gears and wing flaps and the propellers' pitch control (for high-speed helicopters, such as the RACER helicopter).

### *1.2. Helicopter Specificities*

The helicopter PFCS is a specific application for actuators. Linked to safety-critical surfaces, the actuator failure is qualified as "catastrophic" as it leads to the helicopter's crash. The actuation unit must comply with fail safe characteristics. Therefore, the actuation unit must have a redundant topology by force or position summing. The loading spectrum coming from the rotor spinning contains high-frequency content (fundamental at 20 hz minimum). Moreover, the operational pilot demand scenarios are difficult to predict. The required actuation performance is demanding as it combines a significant bandwidth response, reduced plays, high stiffness, and a low mass. The on-board environment is severe with temperature variations within $[-40;\ 85]$ °C, humidity, a salty atmosphere, and vibrations (6 to 20 g, [7]). Finally, concerning the component lifespan, the time between overhauls is required to be from 3000 flight h onwards. This set of specificities highlights the critical function occupied by the actuator in terms of aviation safety.

### *1.3. Electromechanical Actuators*

An electromechanical actuator (EMA) includes components from multiple disciplines. There are mechanical parts (rod ends, bearings and rotary/linear conversion mechanisms, and a clutch), electrical parts (a motor, brake, and clutch), and electronic parts for power and control. The paper [3] presents an example of an EMA in detail and the different possible EMA architectures.

Except for low-power and/or less safety-critical applications (flaps, slats, spoilers, and a trim horizontal stabilizer), the EMA technology is not mature enough yet for primary flight controls [6]. This is essentially because of their lack of accumulated return of experience. The statistical database on components fault modes is poor [8]. EMAs entail some concerns in terms of reliability, risk of failures due to the jamming in the mechanical transmission components, health monitoring (HM) and assessment, and thermal management. The EMA applicability in aerospace has been proved in terms of dynamic performances [8]. In addition, EMAs offer interesting perspectives in terms of maintenance, integration, reconfiguration in case of failure, ease of operation, harsh running environment ($[-50,\ 125]$ °C), and management of power [1,6].

### *1.4. Preliminary Sizing Method*

The preliminary design methodologies can be divided into two phases. The first phase is the system architecture choice, commonly guided by reliability studies, such as those presented in [9–11]. At this level, there are difficulties in taking into account the entire set of design criteria, important to evaluate an architecture. A study with a higher level of details is necessary, especially in the case of the EMA as it includes many constraints and interdisciplinary couplings between components. This is up to the second phase: the preliminary sizing. This phase is mainly based on multidisciplinary optimizations. The models used are usually analytical models or response surface models (RSM) to facilitate the design space exploration and the design optimization.

Some already existing preliminary sizing methodologies can be cited. The references [12,13] present a methodology to select the motor and gearhead of the actuators in the automotive field. The methodology includes a selection based on scaling laws. It outputs graphs showing all feasible motor/gear ratio combinations. In the aeronautic field and regarding the secondary flight control actuators, the paper [14] presents a methodology for the preliminary design of mechanical transmission systems. It is formalized as a constraint satisfaction problem (CSP) with an automated consistency checking and a pruning of the solution space. The mechanical components are modeled by scaling laws. In addition, the paper [10] presents a simulation and an optimization strategy to evaluate two concepts of actuation systems: the conventional hydraulic actuators and the electro hydrostatic actu-

ators (EHAs). Moreover, the paper [15] describes a preliminary design method of EHAs based on multi-objective optimization (MOO) with Pareto dominance. Two objectives are set: the minimization of the mass and the maximization of the efficiency. The weight prediction is achieved using scaling laws, and the efficiency is calculated by a static energy loss model. The method outputs the design parameter, leading to a Pareto front in mass and efficiency.

The scaling laws are good candidates for preliminary design. They are an example of analytical models. They are interesting because they require few data to build them and validate them (existing industrial product ranges). In aerospace, the scaling laws are broadly used in the conceptual design of aircraft, especially regarding aerodynamics, propulsion, structure, and mass [16]. Moreover, the propellers are often described by scaling laws [17–19]. Furthermore, the scaling laws can be used in the field of robotic actuators where low speeds and high torques are usually required [20].

This paper suggests a preliminary sizing methodology applied in the aeronautic field, on helicopters, and on critical EMAs. It contains similar concepts as found in the previously cited literature. Indeed, it includes scaling laws. It includes an optimization where the component selection must satisfy a specification and design constraints while minimizing the actuator total mass. This paper adds its value by the introduction of two elements not considered in the literature yet. The first element is the motor heating based on dynamic criteria extracted from an equivalent representation applied on complex real mission profiles. The helicopter application is more dynamic than the aircraft application, as highlighted in the paper [3]. The second element is the vibratory environment through the actuator housing sizing.

### *1.5. Objective and Outline*

The objective is to set up a design methodology supported by tools estimating the actuator component characteristics for any helicopter PFCS application. The considered EMA architecture is a direct drive in-line EMA. Details regarding this architecture are provided in Section 7.

To address this topic, firstly, this paper briefly presents the proposed global methodology. Secondly, it briefly recalls the tools established in [3] to better understand the actuation need and develops the actuator specification from the given flight data records. Thirdly, the modeling is detailed, limited to the electrical motor and the housing. Finally, the toolbox is applied to two real use cases. One compares two potential redundant topologies of actuation in terms of housing. The other compares the electrical motor characteristics obtained for the specifications of a given helicopter (main rotor and tail rotor).

## 2. Global Methodology

To answer the preliminary design need, this paper offers the global methodology presented in Figure 3. It consists of three main steps:

1. The actuation need must be understood. Flight mission profiles are analyzed. An equivalent actuator specification is synthesized, with key design values corresponding to component specificities.
2. Each actuator component is modeled according to the available inputs.
3. All models are set up into a sizing loop. An optimization algorithm is implemented with the objective of mass minimization.

This methodology takes flight data and high-level project requirements as inputs. It outputs the characteristics of each component necessary to answer the actuation need with a minimized mass.

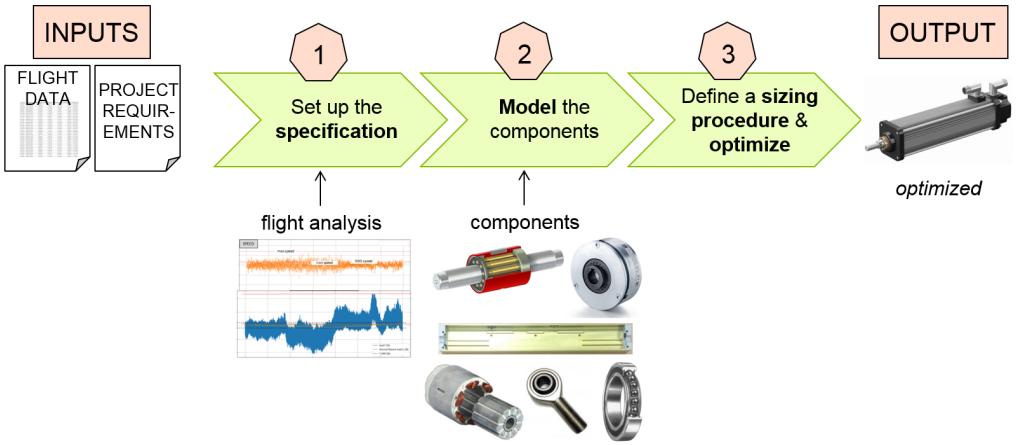


**Figure 3.** Proposed methodology for actuator sizing.

This paper addresses step 1 based on already published work in [3]. It details step 2 focusing only on the tools set up to model two components: the electrical motor and the housing. Step 3 is not explained. The mass minimization is a multidisciplinary design optimization (MDO) problem with numerous interdisciplinary couplings [21–23]. The MDO architecture is chosen to be with a single optimizer. Some variables and constraints are added into the sequencing. This optimization settings correspond to a hybrid individual disciplinary feasible (IDF) architecture and were inspired from [23–25].

## 3. Mission Profile Analysis

To reach the "first time right" objective of a design office, the requirements of any application must be well understood. In that way, the specification is fully representative, and the design is well guided. The EMA application in a PFCS of a helicopter combines three types of difficulties which impede easily writing down its specification. These difficulties are: a set of multidisciplinary design drivers due to the different technologies of the components; an external loading spectrum, coming from the rotor spinning in air, difficult to model; and operational piloting scenarios difficult to predict.

At the time of the project development of unmanned vehicles, a reduced number of short flight-test records with an interesting sampling rate can be available. These data are called mission profiles. They are the most trustful inputs representative of the application requirements. The paper [3] offers to set up an EMA specification based on the analysis of these mission profiles. The offered methodology is briefly recalled in the following subsection.

### *3.1. Methodology*

The methodology offered by [3] has the objective to build the specification whilst simplifying the data analysis for the engineer and keeping them as the decision maker. The methodology is summed up in Figure 4. It is inspired from the work developed on railway trains and aircraft by [26,27]. It contains 4 main steps:

1. Considering the actuator architecture and components to extract a list of key parameters driving the design, called key design drivers.
2. Preparing the data to be analyzed (mission profiles) by filtering and transforming within the temporal or frequency domains.
3. Linking the data to the component key parameters, setting up the mathematical indicators to estimate over mission profiles. Each design driver has its own representative indicator(s).
4. The evaluation of indicators over mission profiles to develop the final EMA specification.

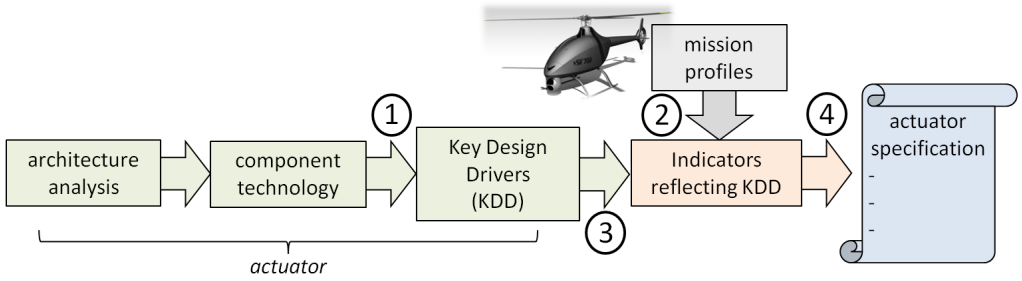


**Figure 4.** Proposed methodology for specification setup.

### *3.2. Estimation over Real Mission Profiles*

The paper [3] illustrates the specification methodology, applying it on real flight data, and emphasizes the specificity of a rotorcraft PFCS for EMA application. It compares the specification of a main rotor actuator (MRA) to the specification of a tail rotor actuator (TRA). The MRA and TRA integration is illustrated in Figure 5. The analysis of the data coming from a real helicopter flight (VSR700, Figure 1) over three flight phases (take-off, cruise, and landing) provides the specifications of the MRA and TRA. In the paper [3], both specifications are compared using ratios elaborated for comparisons. In this paper, both specifications are presented in Table 1. For confidentiality reasons, the values cannot be displayed. Therefore, Table 1 presents ratios such as $X_{MRA}/X_{TRA}$, where $X$ is the concerned specification indicator. These specifications will be the inputs in Section 7.3.

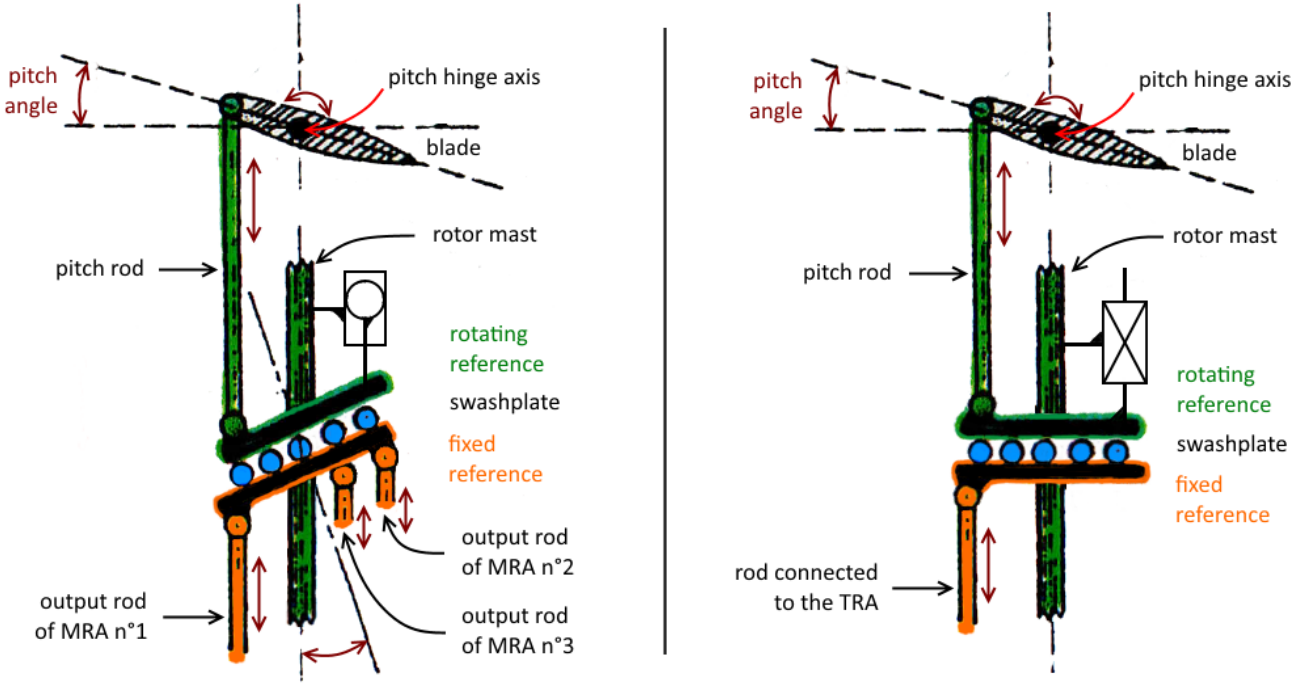


**Figure 5.** Sketch of principle of the main rotor (**left**) and the tail rotor (**right**) on helicopters. The main rotor is responsible for lifting the helicopter weight. The tail rotor ensures the control of the helicopter yaw axis.

At first glance, Table 1 clearly shows that the MRA faces loads roughly 10 times higher than the TRA and moves with an equivalent continuous speed and acceleration roughly 40% lower than the TRA. In the paper [3], the comparison between both applications is emphasized regarding the continuous and maximum loading (from the rotor inertia and external load), the rolling fatigue of the mechanical components, the rotor inertia impact compared to the external load, and the motor loss identification in terms of the continuous motor torque contribution. This paper adds an additional indicator regarding the load-pitting analysis.

**Table 1.** VSR700 specification for MRA and TRA. $a$ is the acceleration, $F$ is the load; they come from measures on the VSR700 helicopter PFCS. $PR = F(t) \cdot a(t)$ is the power rate. The mean power rate $\overline{PR} = | < F(t) \cdot a(t) > |$ takes an absolute value to be conservative. $v_{iron}$ is a mean value of speed representative of motor iron losses. $F_{RMC}$ is an equivalent rolling fatigue load based on $10^6$ cycles. (details in [3]).

| Measures | Indicator | Ratio MRA/TRA [-] |
|---|---|---|
| position | stroke max $s_{max}$ | 1.1 |
| | equivalent distance travelled $L_{eq}$ | 0.5 |
| | speed max $v_{max}$ | 1.1 |
| | speed iron $v_{iron}$ | 0.5 |
| | acceleration max $a_{max}$ | 0.6 |
| | acceleration rms $a_{rms}$ | 0.7 |
| load | load max $F_{max}$ | 7.0 |
| | load rms $F_{rms}$ | 15.1 |
| | load rmc $F_{rmc}$ | 13.6 |
| position & load | power rate mean $\overline{PR}$ | 4.6 |
| | power rate max $PR_{max}$ | 3.0 |
| | pair ($a_{PRmax}$; $F_{PRmax}$) | (0.6; 4.7) |

The pitting load refers to the fluctuating load when the actuator is motionless. This paper suggests estimating the averaged contribution of the load upper frequencies. This can be performed compared to the entire load frequency content. Therefore, the load is separated from its low frequencies using a filter with a cut-off frequency set at the actuator bandwidth value. This resulting load is averaged by the RMS to estimate an equivalent continuous load. This result is normalized by the equivalent continuous load, including all load frequency content. The indicator is $R_p$:

$$R_p = \frac{\left[butter_{HP}[F(t)]\right]_{rms}}{[F(t)]_{rms}} \quad (1)$$

The indicator $R_p$ is evaluated on a nontransient phase of the VSR700 mission profile (Table 2). The indicator shows a higher level of the pitting load in the MRA. This result is understood considering the helicopter rotor architectures (Figure 5). As a piece of information, the MRA selectively controls the blade attack angle during one rotor azimuth. Meanwhile, the TRA simultaneously controls the attack angle of all the blades whatever the azimuth.

**Table 2.** Comparison of the indicator $R_p$ for MRA and TRA applications on VSR700 mission profiles. The indicator is evaluated over steady state flight phases (cruise).

| Domain | Indicator | Unit | MRA | TRA |
|---|---|---|---|---|
| pitting fatigue | $R_p$ | - | 28 | 5 |

## 4. Models for the Preliminary Sizing of EMA

### *4.1. Modeling Overview*

The EMA includes multidisciplinary components. Each of them has multiple and different key design drivers and operational scenarios. The selected components should comply with the actuator specification and ensure a minimized total mass. To answer the need of component selection, a knowledge-based process around component modeling must be set. It covers two levels [28]:

1. The component level: It deals with the determination of component characteristics from a reduced number of parameters to facilitate the optimization. The models involved in it are called the *estimation models* (Figure 6).

2. The system level: It deals with interactions between components, operational scenarios, and component operational limits. The models involved in it are called *simulation models* and *evaluation models* (Figure 6).

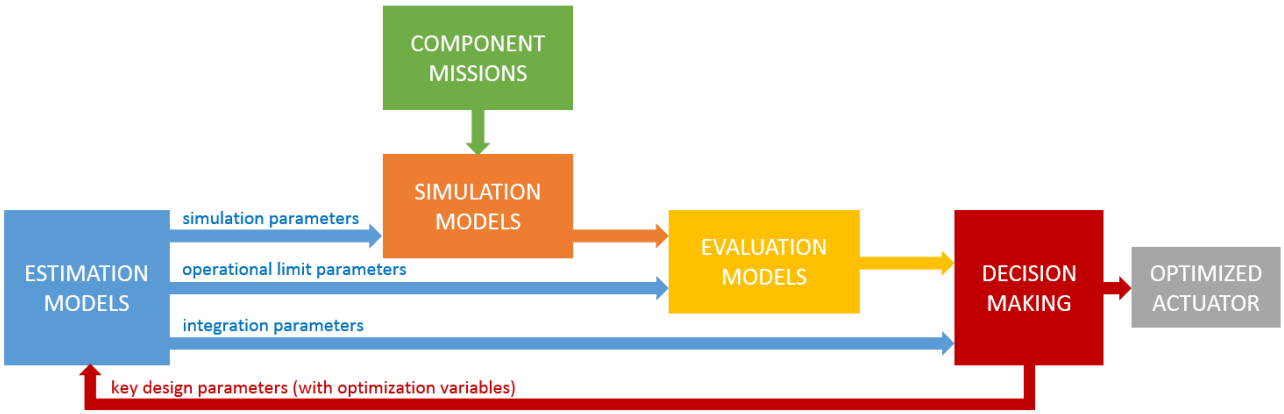


**Figure 6.** Structure of model-based preliminary design.

This paper proposes to focus only on the *estimation models*. To cover the tools setup, only two components are presented. They are those at stake within two onboard specificities: the thermal and vibratory environments. Therefore, the following sections deal with the modeling proposed for the electrical motor and the housing characteristics.

### *4.2. Need of Estimation Models and Approach*

As shown in Figure 6, to start a first iteration in the sizing loop, the main characteristics of each component have to be identified from a reduced set of key parameters. The *estimation models* are introduced for this purpose. Per component, they directly link the primary characteristics, which define the component functionally, to the secondary characteristics, which can be seen as the dimensions and features of the imperfections. Thus, the *estimation models* provide the necessary parameters for the integration study, *simulation models*, and *evaluation models*.

Generally, at the component level, the models link the physical dimensions and characteristics of in-use materials to the primary and secondary characteristics. The design at the component level is an inverse problem which requires the primary characteristics as inputs.

In such a context of multidisciplinary modeling with optimization, a unified modeling approach is required. A dimensional analysis and the Vaschy–Buckingham theorem (Theorem 1) are good candidates for it [29,30]. Indeed, they are extensively used in aerodynamics and fluid mechanics because they provide a more physical and unified framework with a reduced number of parameters. This section shows how they can be extended to other domains, such as the electrical motor and the housing of an EMA.

**Theorem 1** (Vaschy–Buckingham theorem)**.** *Any physical equation dealing with n physical variables depending on k fundamental units (mass, length, time, temperature, charge) can be formulated as an equivalent equation with* $p = n - k$ *dimensionless variables called "π-numbers" built from the initial variables.*

The development steps of an estimation model are presented in Figure 7. The starting point is the expression of one component characteristic $y$ as an algebraic function $f$ depending on the geometrical dimensions and material/physical properties $p_i$. $L$ is a length and $d_i$ the rest of dimensions.

$$y = f(\underbrace{L, d_1, d_2, ...}_{\text{dimensions}}, \underbrace{p_1, p_2, ...}_{\text{properties}}) \quad (2)$$

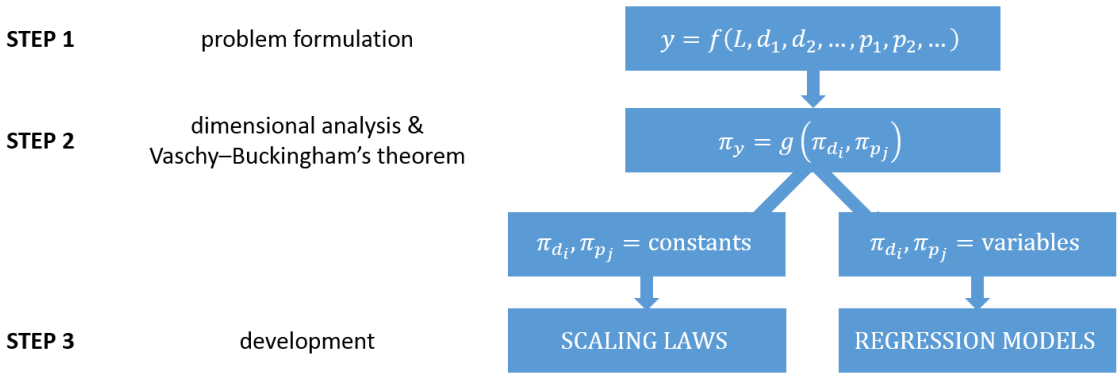


**Figure 7.** Estimation model development steps.

Applying the dimensional analysis and Theorem 1, the problem is rewritten into a reduced number of dimensionless parameters (Equation (3), [31]).

$$\pi_y = g(\underbrace{\pi_{d_1}, \pi_{d_2}, \dots, \pi_{p_1}, \pi_{p_2}, \dots}_{p \text{ variables}}) \text{ with } \begin{cases} \pi_y = y^{c_y} \cdot L^{c_L} \cdot \prod_i p_i^{c_{p_i}} \\ \pi_{d_i} = \frac{d_i}{L} \\ \pi_{p_i} = L^{c_{p_i,0}} \cdot \prod_j p_i^{c_{p_i,j}} \end{cases} \quad (3)$$

The next step is to develop the estimation models based on the $\pi$-groups.

Scaling law formulations are undertaken when the dimensionless numbers $\pi_{d_i}$ and $\pi_{p_i}$ remain constant around a given component product range. This means the geometrical and/or material similarities are satisfied. This is applicable for the electrical motor of the actuator as detailed in the following Section 5.

When the dimensionless numbers $\pi_{d_i}$ and $\pi_{p_i}$ are not considered as constant, the approximation of the function $g$ can be achieved by performing data regressions [31,32]. The data may come from manufacturer product data, test measurements, or finite element simulation results based on design of Experiment (DoE) as presented in Section 6 for the housing vibratory sizing.

## 5. Scaling Laws

In this section, the scaling law theory is firstly developed and then applied to an electrical motor. The actuator sizing requires *estimation models* for its integration (motor dimensions) and its losses (copper and iron losses, inertia).

### *5.1. Fundamentals*

In the literature, scaling laws are also called *similarity laws* or *allometric models* [33]. They estimate the component main characteristics requested for their selection without requiring a detailed design.

Scaling laws are based on three hypotheses:

- Geometric similarity: all the dimensions of the considered component to all the lengths of the component used for reference are constant. Thus, all corresponding aspect ratios are constant: $\pi_{d_i} = \text{constant}$.
- Uniqueness of design drivers: only one main dominant physical phenomenon drives the evolution of the component secondary characteristic $y$. Thus, in most cases, there is not anymore dependency with any $\pi_{p_i}$ (function $g$, Equation (3)).
- Material similarity: all material properties are assumed to be identical to those of the component used for reference. Thus, all corresponding scaling ratios are equal to 1: $\pi_{p_i} = 1$.

Once these assumptions are satisfied, $\pi_y$ is stated to be constant because it depends on constant variables:

$$\pi_y = g(\pi_{d_1}, \pi_{d_2}, ..., \pi_{p_1}, \pi_{p_2}, ...) = \text{ constant} \tag{4}$$

This gives the standard power-law shape of a scaling law:

$$\pi_y = y^{c_y} \cdot L^{c_L} \cdot \prod_i p_i^{c_{p_i}} = \text{ constant } \implies y \propto L^c \tag{5}$$

with $c$ a constant. Then, as proposed by [34], the "star" notation is introduced. It indicates the scaling ratio of a desired component characteristic $x$ by the same characteristic $x_{ref}$ of a component taken as a reference: $x^* = x/x_{ref}$. This component of reference is picked up into the supplier range of the considered product.

Thus, Equation (5) becomes:

$$y^* = L^{*c} \iff \frac{y}{y_{ref}} = \left(\frac{L}{L_{ref}}\right)^c \tag{6}$$

From a single component of reference and a reduced number of parameters (no detailed design required), the scaling laws quickly extrapolate the main characteristics $y_{ref}$ of a known component toward the characteristic $y$ of a possible component of the same technology:

$$y = y_{ref} \cdot \left(\frac{L}{L_{ref}}\right)^c \tag{7}$$

Consequently, the scaling laws level down the complexity of the inversion problem. All the useful relations are easily expressed as a function of a single *key design parameter* (also named *definition parameter*) that is associated with the component under design (Figure 6).

### *5.2. Electrical Motor Scaling Laws*

The previously mentioned approach is applied to the electrical brushless motor. The motor mass-law formulation is detailed hereafter. Beforehand, some hypotheses need to be stated: the main design driver is the maximum continuous winding temperature; the natural convection is the dominant thermal phenomenon; the mean induction in the airgap is constant for a given magnet technology; the number of magnets is constant over the considered product range; and the geometric similarities are verified, and the material and boundary limits similarities are satisfied.

In Figure 8, following the approach mentioned in Section 5.1, step by step, the torque evolution is obtained.

As diameters and lengths are supposed to evolve similarly ($d^* = L^*$, Figure 9), the mass $M$ of the motor is basically approximated by:

$$M = \int \rho_{eq}\, dV \implies M^* = L^{*3} \tag{8}$$

Using the torque expression (prerequisite of Figure 8), the motor mass $M$ becomes:

$$M^* = T^{*3/3.5} \implies M = M_{ref} \cdot \left(\frac{T}{T_{ref}}\right)^{3/3.5} \tag{9}$$

Figure 10 compares the evolution of this law (Equation (9)) to real data from two manufactured motors: Parvex NK [35] and Kollmorgen RBE [36]. It is observed that a single reference of a motor allows to rebuild the evolution of the motor mass for a broad range of torque. This is possible with less than 10% of the mean relative error $\epsilon$.

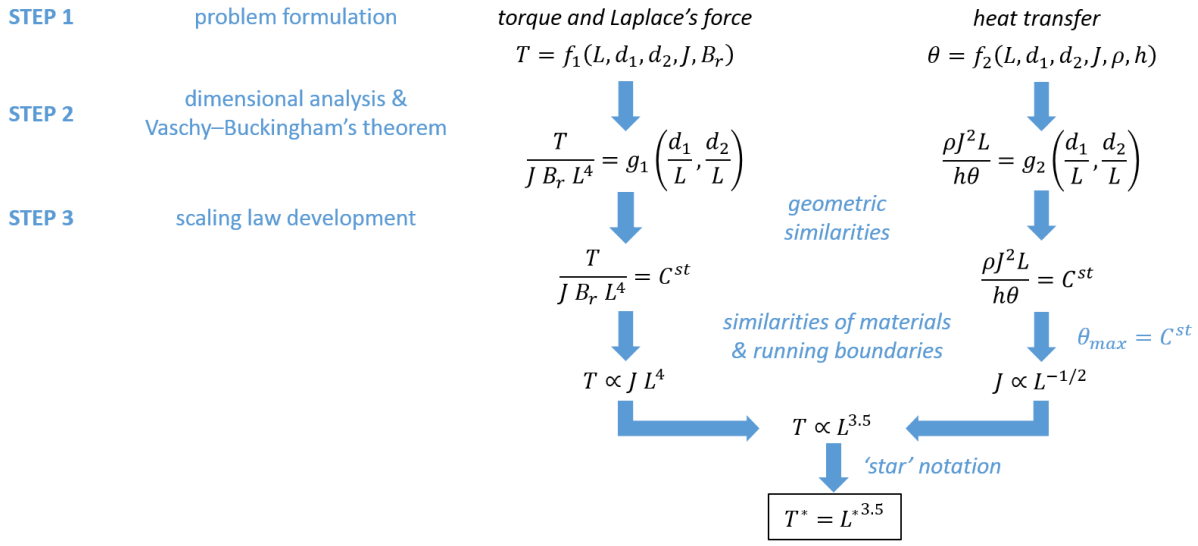


| | | | | | |
|---|---|---|---|---|---|
| $B_r$ | remanent induction of permanent magnets | $[T]$ | $\theta$ | max admissible temperature rise for winding insulation | $[°C]$ |
| $d_i$ | other motor dimensions | $[m]$ | $h$ | convection heat exchange coef. | $[J \cdot K^{-1} \cdot m^{-2}]$ |
| $J$ | current density | $[A \cdot m^2]$ | $L$ | motor length | $[m]$ |
| $\rho$ | copper resistivity | $[ohm \cdot m]$ | $T$ | electromagnetic torque | $[N \cdot m]$ |

**Figure 8.** Electrical motor torque formulation.

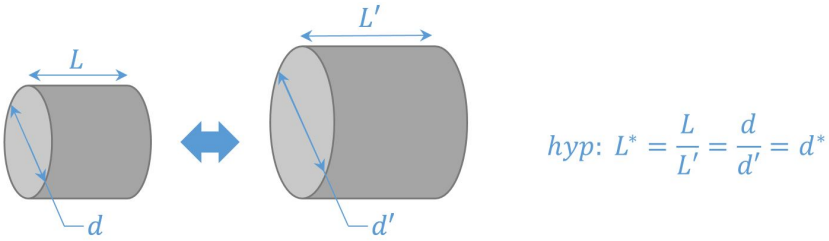


**Figure 9.** Electrical motor: homothety hypothesis.

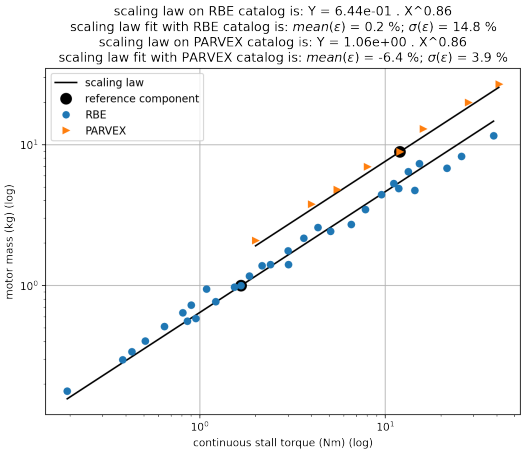


**Figure 10.** Motor mass: scaling law prediction compared to manufacturer catalogs (Parvex NX, Kollmorgen RBE).

In the same way, and following the same hypothesis, the other motor characteristic laws are formulated. Table 3 presents them with their prediction level compared to the Parvex NK catalog. The prediction levels compared to the RBE catalog are presented when data are missing in the Parvex catalog. Both catalogs validate the presented laws.

**Table 3.** Electrical motor scaling law sum up and prediction quality compared to manufacturer catalog data.

| Component Characteristics | Unit | Scaling Law | $\epsilon$ | $\sigma$ | |
|---|---|---|---|---|---|
| ELECTRICAL MOTOR (EM) (brushless, cylindrical) *Note: error estimations performed using PARVEX NK and KOLLMORGEN RBE catalogue ranges ($T \in [0.5; 41]$ Nm)* | | | | | |
| *key design parameter* | | | | | |
| continuous torque | Nm | $T^* = d^{*3.5} = K_m^{*3.5/5}$ | - | - | |
| motor constant | $(\mathrm{N\cdot m})^2/\mathrm{W}$ | $K_m^* = d^{*5} = T^{*5/3.5}$ | - | - | |
| *integration parameter* | | | | | |
| dimensions ($l^* = d^*$) | m | $d^* = T^{*1/3.5} = K_m^{*1/5}$ | 1.1% | 7.5% | |
| mass | kg | $M^* = d^{*3} = T^{*3/3.5} = K_m^{*3/5}$ | 6.4% | 3.9% | |
| *simulation parameter* | | | | | |
| inertia | $\mathrm{kg\cdot m^2}$ | $J^* = d^{*5} = T^{*5/3.5} = K_m^*$ | 0.1% | 20% | |
| copper coef. | $\mathrm{W/(Nm)^2}$ | $\alpha^* = d^{*-5} = T^{*-5/3.5} = K_m^{*-1}$ | 13% | 16% | |
| Joules' losses | W | $P_J^* = d^{*2} = T^{*2/3.5} = K_m^{*2/5}$ | 13% | 16% | |
| iron loss coef. | $\mathrm{W/(rad/s)^{1.5}}$ | $\beta^* = d^{*3} = T^{*3/3.5} = K_m^{*3/5}$ | 6.9% | 19% | |
| resistance | $\Omega/(\mathrm{Nm/A})^2$ | $\mathscr{R}^*/K_t^{*2} = d^{*-5} = T^{*-5/3.5} = K_m^{*-1}$ | 19% | 14% | |
| inductance | $\mathrm{H/(Nm/A)^2}$ | $\mathscr{L}^*/K_t^{*2} = d^{*-3} = T^{*-3/3.5} = K_m^{*-3/5}$ | 0.5% | 17% | |
| number of pole pair | - | $p^* = 1$ | 0% | 0% | |
| *operational limit parameter* | | | | | |
| peak torque | Nm | $T_p^* = d^{*3.5} = T^* = K_m^{3.5/5}$ | 0% | 2.3% | (1) |
| | | $T_{p,mag}^* = d^{*3} = T^{*3/3.5} = K_m^{*3/5}$ | -% | -% | (2) |
| | | $T_{p,th}^* = d^{*4} = T^{*4/3.5} = K_m^{*4/5}$ | 13% | 6.5% | (3) |
| max speed (4) | RPM | $\Omega_{max}^* = d^{*-1} = T^{*-1/3.5} = K_m^{*-1/5}$ | 1.6% | 4.5% | |

(1) Parvex specificity; (2) definition based on magnetic saturation criteria, missing data for validation; (3) definition based on thermal dissipation criteria; be careful that RBE catalog gathers different thermal integrations, $T$ is dependent on them; (4) based on mechanical limitations; $^*$ the 'star' notation: $x^* = x/x_{ref}$.

In Table 3, the motor constant $K_m$ $[(N \cdot m)^2/W]$ is introduced. It is the ratio of the squared torque provided per unit of heat generated. Moreover, it can be found in catalogs with another definition: $[(N \cdot m)/W^{0.5}]$. $K_m$ is an interesting parameter because it directly links the application mechanical need (the required motor torque) with the motor losses without knowing the motor winding characteristics.

As far as the motor losses are concerned, [34,37] mention that the copper and iron losses bound the motor continuous operation domain. The operation domains of electrical motors can be found in [3,33]. Thus, at a steady state, the total heat generated by the electrical motor is the sum of Joules and iron losses, such as:

$$Q_{th} = Q_{Joules} + Q_{iron} = \alpha \cdot T^2 + \beta \cdot f_{elect}^b \tag{10}$$

where $\alpha$ and $\beta$ are, respectively, copper and iron losses coefficients, and $f_{elect}$ the electrical speed. $b$ is a constant depending on the hysteresis and the Eddy's current contributions into iron losses, and [33,37] indicate a mean value of 1.5.

As far as the other components of the actuator are concerned, their scaling laws are found in the publications [20,33].

## 6. Regression Models

In a helicopter context, the resonance frequencies and stress under a vibratory environment is an unavoidable check to perform. This section presents a preliminary vibratory study of a simplified actuator housing. The approach goes through the synthesis of a regression model (also called the surrogate model) to implement into the actuator preliminary sizing loop.

### *6.1. Introduction*

From a purely mechanical point of view, the design of the EMA housing has to focus on the elementary forces acting on the housing, which can be divided into two categories: the static stresses induced by the power transmission to the load, which have low frequencies, and the vibratory stresses induced by the vibratory environment, which have high frequencies ($f \in [5; 2000]$ hz, [7]).

The path of the various static or dynamic loads is represented for a generic actuator in Figure 11.

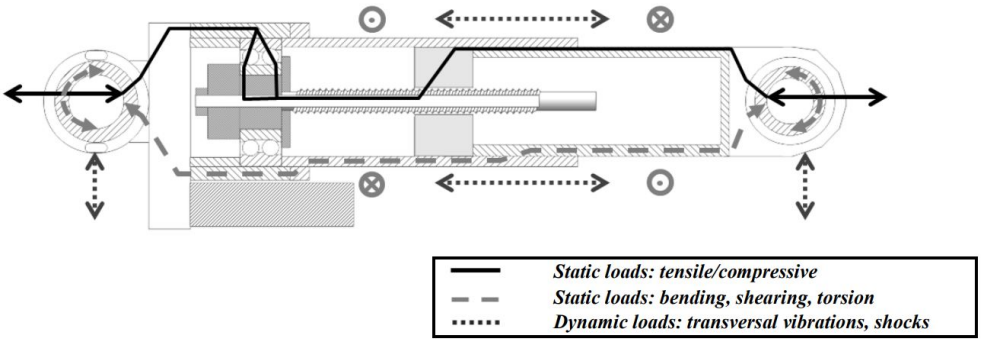


**Figure 11.** Load path in generic EMA [38].

The most significant static loadings are the tensile, compressive, buckling forces. They are transmitted through the rod to the nut, the screw, the bearings, and finally to the housing. The high number of cycles generally requires the fatigue limit of materials to be considered.

The dynamic stress is mainly generated by the transversal vibrations due to the vibratory environment which can generate important mechanical bending stresses. For a long actuator, as it can be for a direct-drive EMA, these stresses are prevailing.

### *6.2. Prior Considerations*

A high-fidelity model of vibratory stress in the housing would be difficult to develop. Indeed, ball bearings and roller screw stiffnesses and plays are unknown and not supplied in datasheets. The contact at the linear bushing level is unclear.

Therefore, we propose a simple model based on some simplifications. The first one concerns the potential mechanical backlash in the actuator assembly and their effect with respect to excitation frequencies. The vibratory amplitude relies on the acceleration level, as illustrated in Table 4.

**Table 4.** Vibratory amplitudes for different acceleration and frequency.

| | | | | | |
|---|---|---|---|---|---|
| number of $g$ | - | 6 | 6 | 20 | 20 |
| acceleration $a$ | $\mathrm{m \cdot s^{-1}}$ | 58.8 | 58.8 | 196 | 196 |
| frequency $f$ | hz | 250 | 50 | 250 | 50 |
| vibratory amplitude $x$ | µm | 24 | 596 | 79 | 1986 |

$$x = \frac{a}{w^2} \quad \begin{cases} x & \text{amplitude [m]} \\ a & \text{acceleration } [\mathrm{m \cdot s^{-2}}] \\ w = 2\pi f & \text{pulsation } [\mathrm{rad \cdot s^{-1}}] \end{cases} \tag{11}$$

The vibratory amplitudes are estimated in Table 4 with Equation (11) regarding commonly used accelerations found in the DO160 standard [7] (6 g for in-cabin equipment, 20 g for an under-swashplate location). The amplitudes can be lower and close to the typical plays. In this case, the vibratory phenomena becomes even more complex. Typical plays at the linear bushing level are roughly 100 µm. The linear bushing or sleeve bearing guides the output rod inside the housing.

To model the effect of the play, we propose a lumped-parameter simulation. It associates one or two mass–spring system(s) excited through an elastogap where the play is modeled as a non-linear stiffness (very low value into the play, and high value far from the play).

In Figure 12, the accelerations stated by the DO–160 standard [7] are plotted in terms of amplitude and frequency.

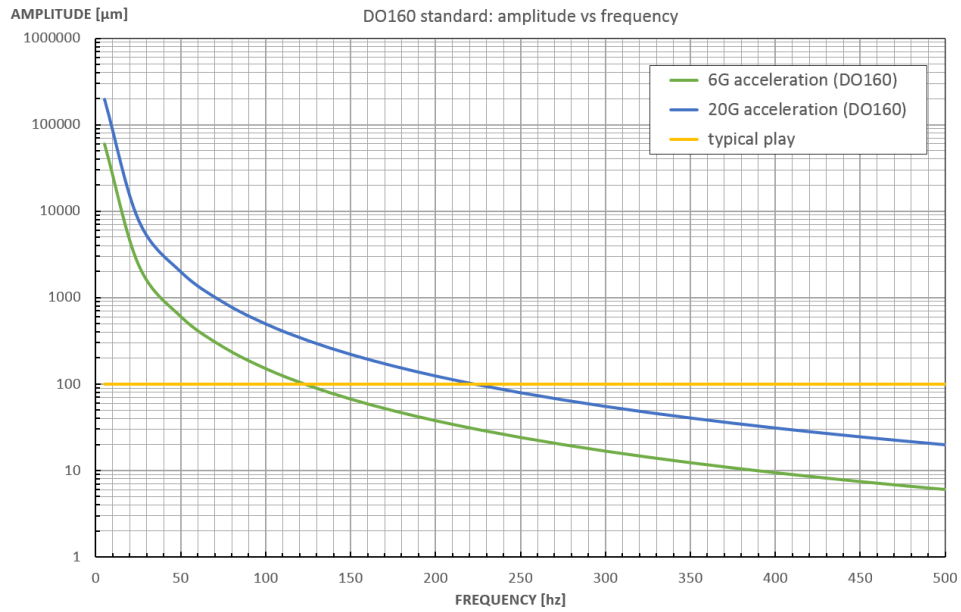


**Figure 12.** DO–160 accelerations: amplitude evolutions with respect to frequencies.

Two cases are studied and illustrated thereafter: *case 1* at 250 hz with $x \leq 100$ $\mu$m and *case 2* at 50 hz with $x \geq 100$ $\mu$m. Both cases consider an acceleration of 6 g.

First of all, the model considers only one mass–spring system.

*Case 1* is simulated in Figure 13. The mass–spring resonance is set at 250 hz and the excitation is around this frequency. No resonance mode of the mass is observed, and the vibratory excitation is 'filtered' by the play.

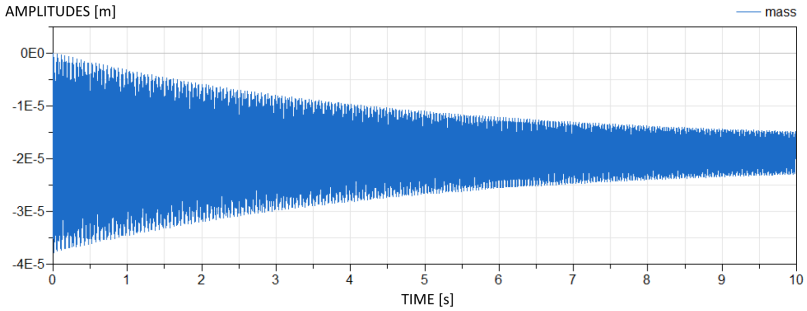


**Figure 13.** Mass amplitudes of the simple mass–spring coupled with play ($f_r = 250$ hz).

*Case 2* is simulated in Figure 14. The mass–spring resonance is set at 50 hz and the excitation is around this frequency. The mass vibrations are more important, and the resonance is observed.

Now, for the plays inside the actuator, the model considers two mass–spring systems linked by an elastogap. Using this model, the displacement of each mass is plotted in Figure 15. For a resonance frequency around 50 hz, the amplitudes are such that the vibrating parts interfaced by the play can be considered as one and a single part.

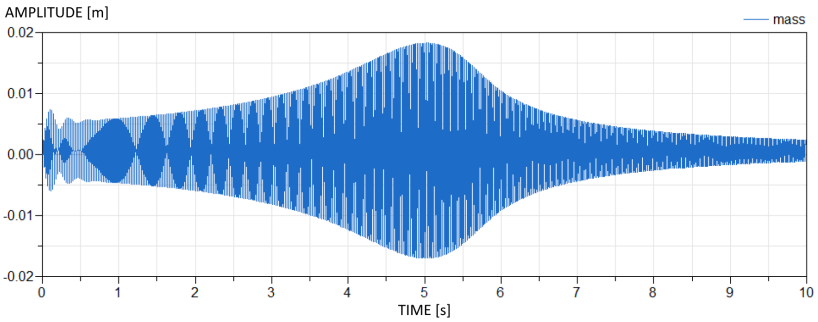


**Figure 14.** Mass amplitudes of the simple mass–spring coupled with play ($f_r = 50$ hz).

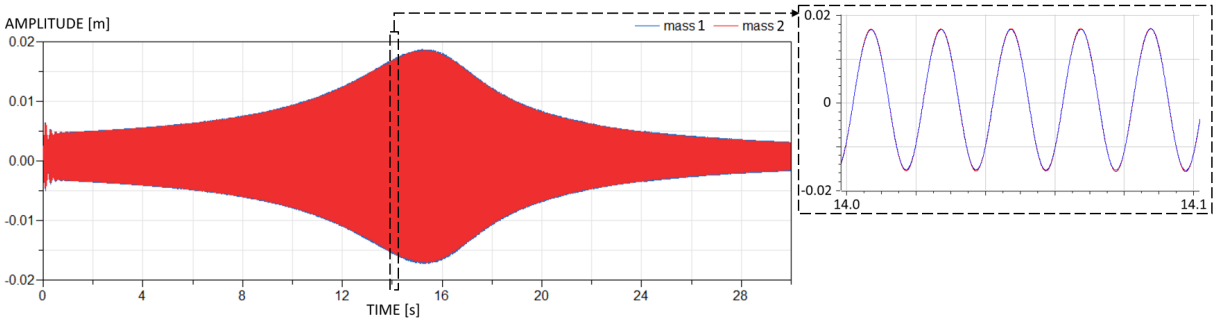


**Figure 15.** Mass amplitudes of the double mass–spring coupled with play ($f_r = 50$ hz).

For a resonance frequency around 250 hz, the vibratory amplitudes are much lower, and the two masses evolve within the play.

As a result, to keep the vibratory amplitudes smaller than the play between the parts, the resonance frequencies must be high (e.g., $\geq$200 hz; this limit depends on the amplitude of the acceleration). It is not the case for long and narrow actuators as direct-drive actuators can be. The resonance frequencies are low.

Thus, some simplifications can be introduced into the estimations of stresses of the actuator envelop under vibratory excitations. We propose to suppose, for housings with low resonance frequency, that the plays are negligible compared to the vibratory amplitudes. Consequently, the contact with linear bushing is modeled as an infinitely rigid contact.

### *6.3. Hypothesis*

Now, an FEM model of reduced parameters is developed in order to represent it by a surrogate model. Some more hypotheses are formulated.

A simplified geometry is considered (Figure 16): two hollowed cylinders, one in the other. The connection between them is assumed to be perfect. The set (motor, brake, connectors, and bearings) is supposed to be a cylinder of 1/3rd of $L_a$ with an equivalent density. This equivalent mass is modeled with Young's low modulus (1/10th of aluminium modulus). This choice is conservative; it is so as to not impact the stiffness of the housing.

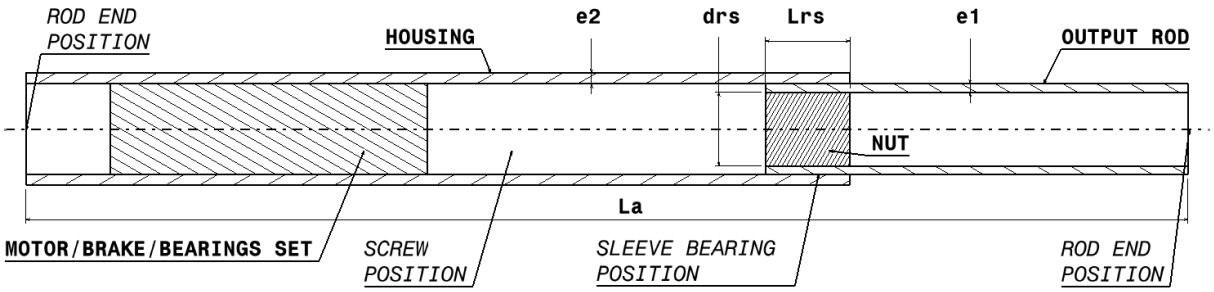


**Figure 16.** Actuator simplified geometry for modal analysis.

The housing and output rod are set with the same material properties (aluminium). Their lengths are, respectively, supposed to be 2/3rd and 1/3rd of $L_a$.

The nut is modeled as a full cylinder with 90% steel density (7000 kg·m$^{-3}$) to consider the air content between the rollers. The geometry of the nut evolves with the geometrical similarity assumption (scaling law). The cylinder representing the nut is modeled using a low Young's modulus (1/10th of steel modulus) so as to not influence the stiffness of the structure.

The rod ends allow rotation with no friction.

The antirotation key and the sealing leap at the interface output rod with housing are not modeled.

The three following sections develop a surrogate model using the surrogate modeling technic suggested in the paper [31].

### *6.4. Problem Formulation*

Under vibration, the system can be associated to a basic damped mass–spring model. Figure 17 presents this model with $U$ (m) the displacement of an equivalent mass $M_{eq}$ (kg) evolving according to an excitation force $F$ (N), a stiffness $K_{eq}$ (N · m$^{-1}$), and a damping $C_{eq}$ (N · m$^{-1}$ · s).

The stress is linearly linked to the displacement:

$$\sigma = k_\sigma \cdot U \qquad\qquad k_\sigma = \frac{\sigma_0}{U_0} \tag{12}$$

with $\sigma_0$ $[Pa]$ and $U_0$ [m], the maximum stress and the maximum displacement at resonance frequency.

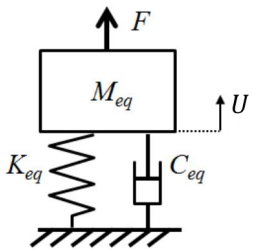


**Figure 17.** Mass–spring model.

Newton's second law applied to the moving body enables the Laplace function between the displacement $U(t)$ and the excitation load $F(t)$ to be estimated, such as:

$$\frac{U(p)}{F(p)} = \frac{1}{M_{eq} \cdot p^2 + C_{eq} \cdot p + K_{eq}} = \frac{1/K_{eq}}{p^2/\omega_r^2 + 2 \cdot \xi \cdot p/\omega_r + 1} \tag{13}$$

Considering an excitation of the mass with a sinusoidal force $F(t) = F_0 \cdot sin(\omega \cdot t)$, the maximum displacement at the first resonance mode is:

$$U_0 = \frac{1}{2 \cdot \xi} \cdot \frac{F_0}{K_{eq}} = \frac{Q_m \cdot F_0}{K_{eq}} \qquad\qquad \xi = \frac{C_{eq}}{2 \cdot \sqrt{K_{eq} \cdot M_{eq}}} \approx \frac{1}{2 \cdot Q_m} \tag{14}$$

where $Q_m$ is the mechanical quality coefficient.

The article [38] reports that tests performed on industrial prototypes show a wide range of practical values for the equivalent mechanical quality coefficient $Q_m$. In addition, it reports that experiments give typical values for $Q_m$ between 10 and 50, depending on the application and boundary conditions. For structural dynamic models, in the absence of better information, it is normally acceptable to assume a value of $Q_m = 30$ (according to [39]).

The equivalent force $F_0$of the acceleration effect can be evaluated thanks to an equivalent work $\mathscr{W}_0$ [40,41]:

$$\mathscr{W}_0 = F_0 \cdot U_0 = \iiint_{\mathscr{V}} u_0 \cdot a \cdot \rho \cdot d\mathscr{V} \tag{15}$$

with $u_0(x)$ the deflection of the actuator envelop, $a$ the amplitude of the vibratory sinusoidal acceleration. A mass $M_{acc}$ subjected to the acceleration can be defined:

$$F_0 = M_{acc} \cdot a \qquad\qquad M_{acc} = \frac{\iiint_{\mathscr{V}} u_0 \cdot \rho \cdot d\mathscr{V}}{U_0} \tag{16}$$

The mass subjected to the acceleration is not identical to the mass expressing the kinetic energy, $M_{eq}$, defined such as [40,41]:

$$\frac{1}{2} \cdot M_{eq} \cdot V_0^2 = \iiint_{\mathscr{V}} \frac{1}{2} \cdot \rho \cdot v_0^2 \cdot d\mathscr{V} \tag{17}$$

with, at the first mode resonance, $V_0$ the speed of $M_{eq}$ and $v_0(x)$ the speed of each point of the actuator deflection. The speeds can be defined such as:

$$v = w_0 \cdot u \qquad\qquad V = w_0 \cdot U \tag{18}$$

Thus, we can easily define the equivalent mass such as:

$$M_{eq} = \frac{\iiint_{\mathscr{V}} \rho \cdot u_0^2 \cdot d\mathscr{V}}{U_0^2} \tag{19}$$

The following ratio is introduced:

$$k_{acc} = \frac{M_{acc}}{M_{eq}} = \begin{cases} U_0 \cdot \frac{\iiint_{\mathscr{V}} u_0 \cdot d\mathscr{V}}{\iiint_{\mathscr{V}} u_0^2 \cdot d\mathscr{V}} & \text{if } \rho \text{ is constant} \\ U_0 \cdot \frac{\iiint_{\mathscr{V}} u_0 \cdot \rho \cdot d\mathscr{V}}{\iiint_{\mathscr{V}} u_0^2 \cdot \rho \cdot d\mathscr{V}} & \text{if } \rho \text{ is not constant} \end{cases} \tag{20}$$

and the maximum displacement at the resonance can be approximated as it follows:

$$U_0 = \frac{Q_m \cdot k_{acc} \cdot M_{eq} \cdot a_0}{K_{eq}} = \frac{Q_m \cdot k_{acc} \cdot a_0}{\omega_0^2} \tag{21}$$

with $\omega_0^2 = K_{eq}/M_{eq}$ the resonance angular frequency.

### *6.5. Dimensional Analysis*

As seen in Section 5, the use of a dimensional analysis and Buckingham's Theorem enable to reduce the number of variables expressing a physical problem. Here below, this approach is developed for the vibratory use case. By simplification and for a reduced number of parameters, a constant density $\rho$ is assumed all along the actuator (Equation (20)).

The link between stress and displacement evolves according to the following variables:

$$\frac{\sigma}{U} = k_\sigma = f(E, d_{rs}, L_a, e_1, e_2, L_{rs}) \tag{22}$$

which can be rewritten with the following dimensionless numbers:

$$\pi_{k_\sigma} = \frac{\sigma \cdot d_{rs}}{U \cdot E} = f\left(\frac{L_a}{d_{rs}}, \frac{e_1}{d_{rs}}, \frac{e_2}{d_{rs}}, \frac{L_{rs}}{d_{rs}}\right) \tag{23}$$

The resonance angular frequency evolves according to:

$$\omega_0 = g(E, \rho, d_{rs}, L_a, e_1, e_2, L_{rs}) \tag{24}$$

which can be rewritten with the following dimensionless numbers:

$$\pi_{\omega_0} = \omega_0 \cdot \left(\frac{\rho}{E}\right)^{1/2} \cdot d_{rs} = g\left(\frac{L_a}{d_{rs}}, \frac{e_1}{d_{rs}}, \frac{e_2}{d_{rs}}, \frac{L_{rs}}{d_{rs}}\right) \tag{25}$$

The stress under a vibratory acceleration can be expressed as:

$$\sigma = k_\sigma \cdot U = k_\sigma \cdot \frac{Q_m \cdot k_{acc} \cdot a}{\omega_r^2} = \sigma_0 \cdot Q_m \cdot a \cdot \frac{\iiint_{\mathcal{V}} u_0 \cdot d\mathcal{V}}{\iiint_{\mathcal{V}} u_0^2 \cdot d\mathcal{V}} \tag{26}$$

The stress evolves according to:

$$\sigma = h(k_\sigma, \omega_0^2, a, Q_m) \tag{27}$$

which can be rewritten as:

$$\pi_0 = \frac{\sigma}{Q_m \cdot a \cdot d_{rs} \cdot \rho} = h\left(\frac{L_a}{d_{rs}}, \frac{e_1}{d_{rs}}, \frac{e_2}{d_{rs}}, \frac{L_{rs}}{d_{rs}}\right) \tag{28}$$

The expression of the stress is thus only function of four aspect ratios. One of these aspect ratios, $L_{rs}/d_{rs}$, can be assumed to be constant because of the geometrical similarity assumption used for roller screw component sizing (scaling law).

The final expression of the stress is a function dependent of three dimensionless quantities:

$$\pi_0 = g(\pi_1, \pi_2, \pi_3) \begin{cases} \pi_0 = \sigma/(Q_m \cdot a \cdot d_{rs} \cdot \rho) \\ \pi_1 = L_a/d_{rs} \\ \pi_2 = e_1/d_{rs} \\ \pi_3 = e_2/d_{rs} \end{cases} \tag{29}$$

It remains to determine this function $g$. The following section does the job.

### *6.6. FEM Software Model*

Using a software for computation by finite elements, a model is parametrized according to the previous considerations and hypotheses. It enables to obtain:

- The resonance frequency $f_r$ or the resonance angular frequency $\omega_r$.
- The modal form characterized by a maximal displacement $U_0$.
- The corresponding maximum stress $\sigma_0$. The maximum stress is identified to be on the output rod tube ($e_1$ thickness).

The intersection of both cylinders has been taken care of by smooth and arced geometries to avoid numerical stress constraints. The boundaries are pinned at each extremity of the actuator model. The deflection is allowed within the plane of the section presented in Figure 18.

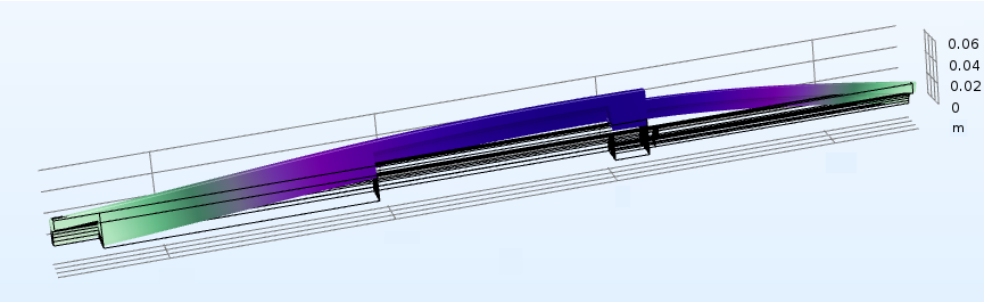


**Figure 18.** Modal analysis of the simplified actuator geometry.

The tandem topology of actuation is largely used in the aeronautic field because it complies with safety aviation rules. This topology involves two actuators stuck to each other at their basement, and their extension is in opposite directions (more details provided in Section 7.2). This topology increases the total length of the actuation unit. To consider this use case, another surrogate model needs to be developed.

The FEM model for the single actuator is reused. The boundary conditions are changed. A symmetry constraint is applied to the geometry at the actuator basement. The stress is picked up onto two critical points: at the interface between both actuators and at the interface between the output rod and the housing. Two surrogate models are expressed to determine the value of $\pi_0$ for each of these points.

### *6.7. DOE and Surrogate Synthesis*

A design of experiments (DoE) is realized with $e_1$, $e_2$, $d_{rs}$, and $L_a$. The simulations (a modal analysis) generate the variable of interest $\pi_0$.

The dependent variable of the problem is approximated thanks to a linear regression (response surface model (RSM)) where the development takes into account a mean value, a first-order member (which represents the main effects of the problem), a combined member (representing the interactions), and a second-order member to consider further effects. The development takes the following form:

$$\pi_0 = \underbrace{a_0}_{\text{mean value}} + \underbrace{\sum a_i \pi_i}_{\text{main effect}} + \underbrace{\sum a_{ij} \pi_i \pi_j}_{\text{interactions}} + \underbrace{\sum a_{ii} \pi_i^2}_{\text{high order effect}} \tag{30}$$

The VPLM methodology (Variable Power-Law Metamodel) [31] is applied. A log transformation on variables is performed for the linearization which gives the form:

$$log(\pi_0) = a_0 + \sum a_i log(\pi_i) + \sum a_{ij} log(\pi_i) log(\pi_j) + \sum a_{ii} log(\pi_i)^2 \tag{31}$$

and can be rewritten as:

$$\pi_0 = 10^{a_0} \prod_{i=1}^{n} \pi_i^{\,a_i + a_{ii} log(\pi_i) + \sum_{j=i+1}^{n} a_{ij} log(\pi_j)} \tag{32}$$

This variable power-law form enables to deal with the large variation range of the dependent and independent variables.

The data set coming from the DoE is shared in two sets: one for the regression procedure so as to determine the coefficients $a_i$ and $a_{ij}$ (Equation (31)) and the other for the test of the final surrogate.

The regression gives the following surrogate model which determines the value of $\pi_0$ for the housing of a single actuator:

$$\begin{aligned} log_{10}(\pi_0) =& 68 \cdot log_{10}\left(\frac{L}{d}\right)^2 \cdot \frac{1}{293} + 64 \cdot log_{10}\left(\frac{L}{d}\right) \cdot log_{10}\left(\frac{e_1}{d}\right) \cdot \frac{1}{973} + log_{10}\left(\frac{L}{d}\right) \cdot log_{10}\left(\frac{e_2}{d}\right) \cdot \frac{1}{1000} \\ &+ 1099 \cdot log_{10}\left(\frac{L}{d}\right) \cdot \frac{1}{984} + 86 \cdot log_{10}\left(\frac{e_1}{d}\right)^2 \cdot \frac{1}{657} + 229 \cdot log_{10}\left(\frac{e_1}{d}\right) \cdot log_{10}\left(\frac{e_2}{d}\right) \cdot \frac{1}{884} \\ &- 101 \cdot log_{10}\left(\frac{e_1}{d}\right) \cdot \frac{1}{249} + 538 \cdot log_{10}\left(\frac{e_2}{d}\right)^2 \cdot \frac{1}{685} + 670 \cdot log_{10}\left(\frac{e_2}{d}\right) \cdot \frac{1}{359} + \frac{527}{551} \end{aligned} \tag{33}$$

with $L$ the length $L_a$ and $d$ the diameter $d_{rs}$.

The two other surrogate models developed for the tandem actuator housing are shown in Appendix A.

### *6.8. Validation*

In Figure 19, the prediction of the surrogate model (Equation (33)) is compared to the FEM simulation result data set. The prediction level is satisfying with $R^2 > 99\%$. The two other housing surrogate models show the same prediction level quality.

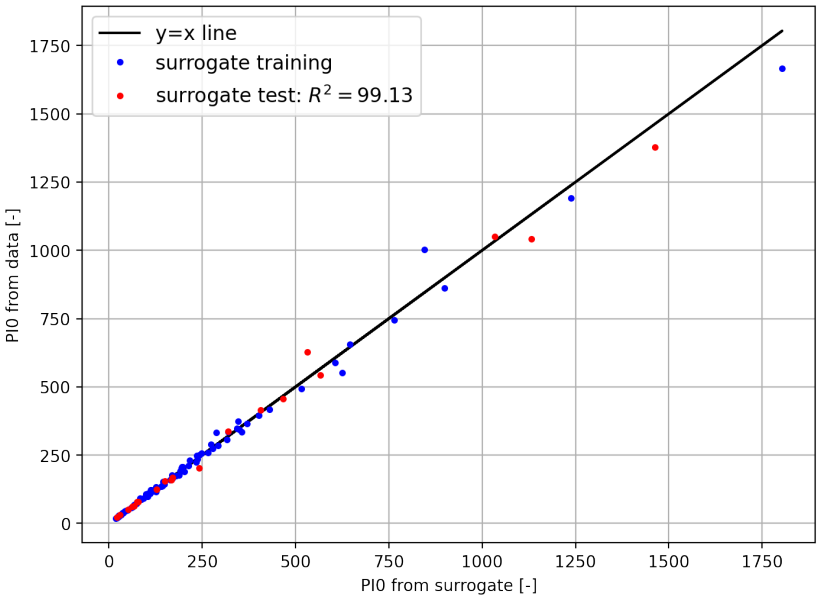


**Figure 19.** Surrogate model for single actuator housing: $\pi_0$ results (Equation (33)).

## 7. Results

In this section, some real application cases are discussed to illustrate the previously presented methodologies.

The methodology mentioned in Section 2 is implemented as a graphical user interface (GUI) web application based on a Jupyter Notebook calling functions through Python scripts. The GUI is developed with a dashboard named Voila. The tools developed in Section 4 are included with an optimization algorithm (differential evolution). Different specifications from real application cases are executed into this sizing code and the output results are presented. These specifications are arbitrary or linked to redundant topologies of actuation and to two different helicopter use cases: the main rotor and the tail rotor.

The considered actuator architecture is provided in Figure 20. In a housing (H), a frameless PMSM electrical motor (EM) is guided by two bearings (BB1 and BB2). BB1 is an angular contact double-row ball bearing; it withstands the entire axial load. BB2 is a radial contact single-row ball bearing; it ensures the motor rotor alignment. The electrical motor (EM) is linked to a screw mechanism (SM). In this paper, a planetary roller-screw (PRS) technology is considered. The screw spins and the nut moves linearly. The output rod (OR) is fixed onto the nut of the SM. A rod end (RE) (also named a spherical bearing) ensures the connexion of the output rod with the loading device. In this paper, the loading device is the helicopter swashplate. On the other side, another rod end (RE) ensures the connexion of the actuator housing (H) with a frame. Finally, the electromagnetic brake (EMB) satisfies a safety function in the case of a electricity supply cut-off.

For confidentiality matters, the inputs and results are presented as ratios of quantities. The observation of the sizing evolutions is the focus point of this section.

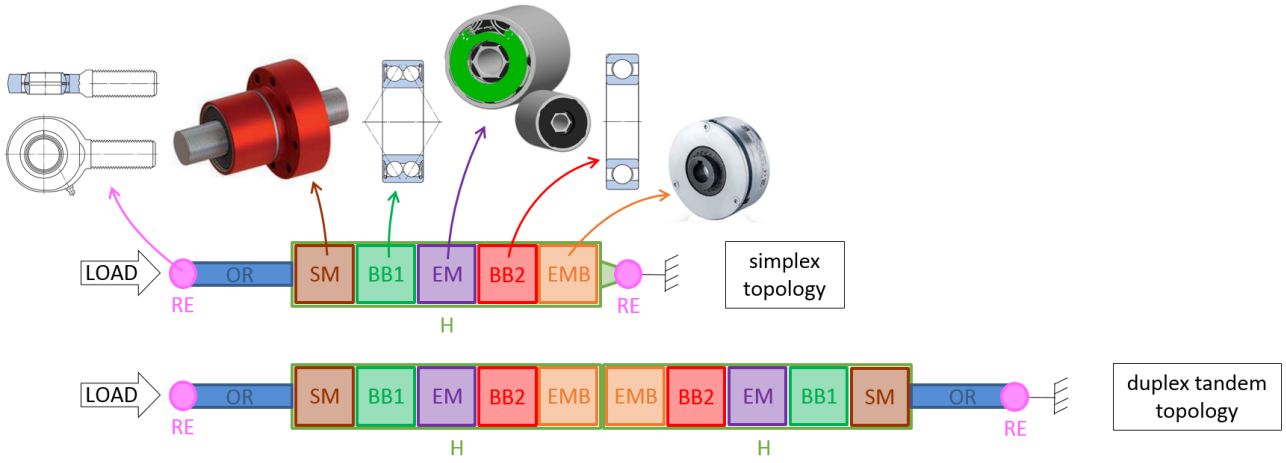


**Figure 20.** Actuator architecture considered in results.

### *7.1. Arbitrary Sizings*

We suggest presenting some preliminary sizing results from an arbitrary specification. The arbitrary specification and the associated design hypothesis are given in Table 5. The actuator sizing results regarding the simplex topology (Figure 20) are available in Table 6, in the column named *sizing A*. To show the sensitivity of the values of the static load, stroke, and acceleration (RMS), the arbitrary specification is run again three times with, every time, a modification of one indicator value. *Sizing B* includes the arbitrary static load multiplied by 2. *Sizing C* includes the arbitrary stroke multiplied by 4. *Sizing D* includes the arbitrary RMS acceleration multiplied by 2.

The following lines comment the sizing results presented in Table 6. Although the mechanical components are not the focus point of this article, they must be mentioned to better understand the sizing choices performed by the optimization.

The arbitrary specification leads a design of the mechanical components mainly guided by the fatigue criteria (*sizing A*). This means that the static load criteria are satisfied with margins. Moreover, because of the low heat-transfer coefficient, the low emissivity, and the significant RMS acceleration level (see Table 5), the electrical motor design is driven by the heat dissipated through the actuator skin, by convection and radiation.

**Table 5.** Arbitrary specification and its design hypothesis.

| Specification | Unit | Value | Design Hypothesis | Unit | Value |
|---|---|---|---|---|---|
| stroke $s_{max}$ | mm | 50 | all safety coefficients | - | 1 |
| equivalent distance traveled $L_{eq}$ | km | 100 | skin temperature max | °C | 100 |
| speed max $v_{max}$ | $m \cdot s^{-1}$ | 0.2 | housing heat-transfer coef. (convection) | $W \cdot m^{-2} \cdot K^{-1}$ | 5 |
| speed iron $v_{iron}$ | $m \cdot s^{-1}$ | 0.1 | housing emissivity | - | 0.4 |
| acceleration max $a_{max}$ | $m \cdot s^{-2}$ | 5 | housing & output rod density | $kg \cdot m^{-3}$ | 7800 |
| acceleration rms $a_{rms}$ | $m \cdot s^{-1}$ | 1 | housing & output rod thickness min | mm | 1 |
| load max $F_{max}$ | kN | 3 | housing & output rod fatigue stress | MPa | 500 |
| load rms $F_{rms}$ | kN | 1 | quality coefficient $Q_m$ | - | 30 |
| load rmc $F_{rmc}$ | kN | 1 | vibratory acceleration | $m \cdot s^{-2}$ | 98 |
| load dynamic peak-to-peak $F_{pitting}$ | kN | 1 | bus voltage max | Vdc | 110 |
| power rate mean $\overline{PR}$ | $W \cdot s^{-1}$ | 1 | motor phase current max | Apeak-sine | 10 |
| pair $(a_{PRmax}; F_{PRmax})$ | $(m \cdot s^{-2}; kN)$ | (3; 1.5) | time-to-stop speed (EMB) | s | 0.05 |
| equivalent load mass | kg | 50 | shaft density | $kg \cdot m^{-3}$ | 7800 |
| ambient temperature | °C | 25 | | | |
| load frequency | hz | 20 | | | |
| total lifespan $t_{life}$ | hours | 20,000 | | | |

**Table 6.** Sizing results from the arbitrary specification.

| | | Value of Characteristics | | | |
|---|---|---|---|---|---|
| **Component** | **Characteristic** | **Sizing A** | **Sizing B ($F_{max}$ X2)** | **Sizing C ($s_{max}$ X4)** | **sizing D ($a_{rms}$ X2)** |
| *MECHANICAL COMPONENTS* | | | | | |
| screw mechanism (SM) | thread lead (mm/rev) | 3.1 | 3.1 | 3.5 | 3.8 |
| SM (nut, screw), BB1, BB2, and RE (x2) | total mass (kg) | 0.72 | 0.72 | 0.91 | 0.65 |
| *ELECTRICAL COMPONENTS* | | | | | |
| electrical motor (EM) | inertia (kg · m$^2$) | $7.6 \times 10^{-5}$ | $1.1 \times 10^{-4}$ | $4.9 \times 10^{-5}$ | $1.1 \times 10^{-4}$ |
| | external diameter (mm) | 60 | 64 | 55 | 65 |
| | motor constant $K_m$ ($10^{-2}$ (Nm)$^2$/W) | 4.6 | 6.3 | 3.0 | 6.8 |
| | torque constant $K_t$ (Nm/Arms-sine) | 0.23 | 0.26 | 0.24 | 0.26 |
| | mass (kg) | 1.1 | 1.4 | 0.87 | 1.4 |
| electromagnetic brake (EMB) | inertia (kg · m$^2$) | $1.0 \times 10^{-5}$ | $2.0 \times 10^{-5}$ | $1.0 \times 10^{-5}$ | $1.3 \times 10^{-5}$ |
| | mass (kg) | 0.72 | 1.1 | 0.73 | 0.83 |
| *ACTUATOR* | | | | | |
| housing (H) | thickness (mm) | 1.1 | 1.2 | 4.6 | 1.1 |
| | mass (kg) | 1.8 | 2.0 | 4.1 | 1.9 |
| output rod (OR) | thickness (mm) | 1.4 | 1.4 | 3.9 | 1.4 |
| | mass (kg) | 0.14 | 0.14 | 0.78 | 0.14 |
| actuator (simplex) | total mass (kg) | 4.6 | 5.5 | 7.5 | 5.1 |

In *sizing B*, the increase in the static load stands in the static load margin of the mechanical components; their sizing remains unchanged. However, the electromagnetic brake (EMB) must stop a higher torque. Indeed, the torque to stop in an emergency relies on two specified values: the static load converted by the indirect efficiency of the screw (SM) and the screw maximum speed to stop within the specified time. Doubling the static load, the EMB requires to develop a higher braking force. It is bigger then. This involves the increase in the EMB disk inertia that sums to the total rotating inertia. Thus, a higher electrical motor performance is required. Because of the increased length of the electrical components, the housing is heavier.

Increasing the specified stroke (*sizing C*) makes the actuator longer. The ratio diameter by length is decreased. The housing and the output rod must have their thickness increased to withstand the vibratory accelerations. The screw of the SM is longer, involving an additional mass. What is more, the increased actuator length offers a more extended outer surface for dissipating the heat generated by the motor. The electrical motor (EM) can have lower performances if the thread lead is increased. The EM has a reduced mass then.

The motor heat generation is based on a continuous torque. The RMS acceleration highly contributes to this torque. Doubling the specified RMS acceleration (*sizing D*) involves an important specified continuous torque. The motor size must be increased to satisfy this specification. Increasing the lead limits the motor size increase for a reduced mass. With a bigger motor, the rotating inertia is higher and the EMB is required to be bigger. Moreover, increasing the lead reduces the fatigue phenomenon applied to the mechanical components. The mechanical components are chosen with slightly smaller fatigue capabilities. They are slightly smaller then. Moreover, the sized electrical components make the actuator longer. Thus, the housing (H) is slightly heavier.

### *7.2. Sizing of Redundant Topologies of Actuation*

There are mainly two redundant topologies of actuation [6,42,43]. The first one is the force summing where the failed or passive actuator shall be free in motion. In this case, the actuator must be equipped with a clutch or any breaking fuse system. The second one is the position summing where the failed or passive actuator shall be locked from motion. In

this case, the actuators must be equipped with a power-off brake. The position summing topology can be seen with actuators either installed in tandem (as presented in Figure 21a) or in parallel (Figure 21b). The tandem configuration is the one most commonly found in aeronautics. This equips the PFCS of fighter aircrafts and helicopters and the SFCS of commercial aircrafts (except the spoiler) [6]. Meanwhile, the parallel configuration is much less used [6].

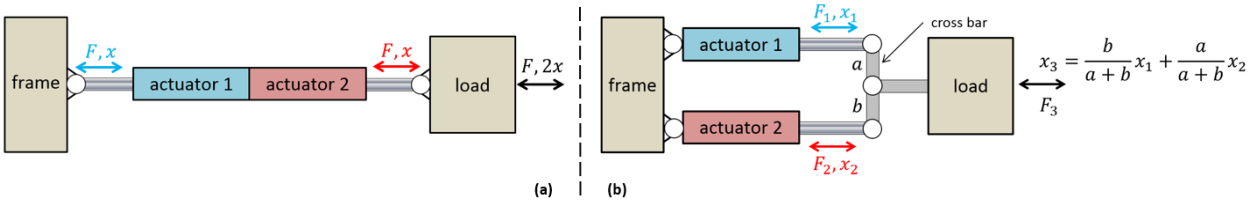


**Figure 21.** Redundant topologies of actuator in position summing (passive/failed actuator shall be locked). (**a**) One tandem actuator, (**b**) two simplex actuators linked by a cross bar ($a = b$ considered, $F_1 = F_2 = F_3/2$).

This paper proposes to study the impact on the housing mass and output rod mass involved in the consideration of topology (b) compared to topology (a) (Figure 21). It is clear that topology (b) introduces potential additional plays and wear points compared to topology (a). However, it is important to estimate if this topology involves any mass gain that would compensate these drawbacks.

From tandem to parallel topologies, the force is halved; meanwhile, the stroke, speed, and acceleration are doubled. The work produced by the actuator remains the same.

The bar chart presented in Figure 22 presents the sizing results involved in both actuation topologies. The results are given as a ratio, with the sizing results obtained for a simplex actuator not equipped with any electromagnetic brake.

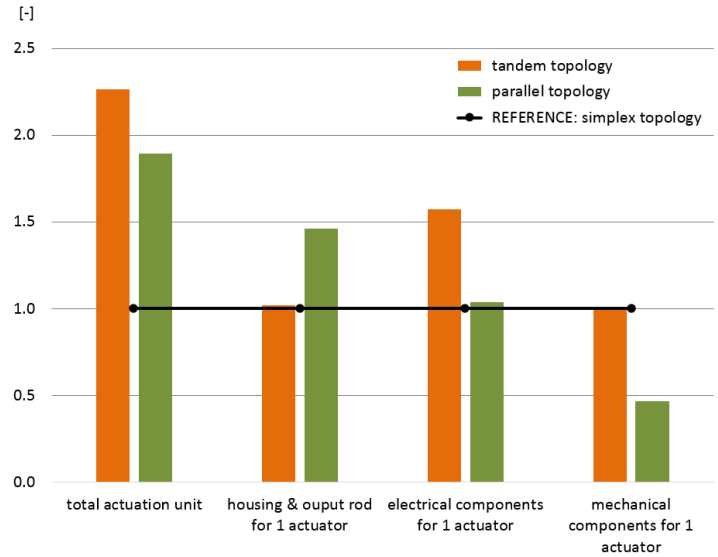


**Figure 22.** Mass evolution of tandem or parallel topologies compared to simplex topology.

As the parallel topology requires a doubled stroke and half load, the actuator is longer and smaller in diameter than in the tandem topology. The thicknesses of the housing and the output rod are nearly doubled. The mass of the set (housing and rod) results to be half heavier than the one of the tandem topology. The parallel topology shows electrical components and mechanical ones with reduced characteristics and reduced masses compared to the tandem topology. Therefore, the contribution of the set (housing and rod) mass on the total actuator mass is much higher for the parallel topology. Figure 23 confirms it with a contribution of a third of the actuator mass concerning the tandem topology against more than half the actuator mass concerning the parallel topology.

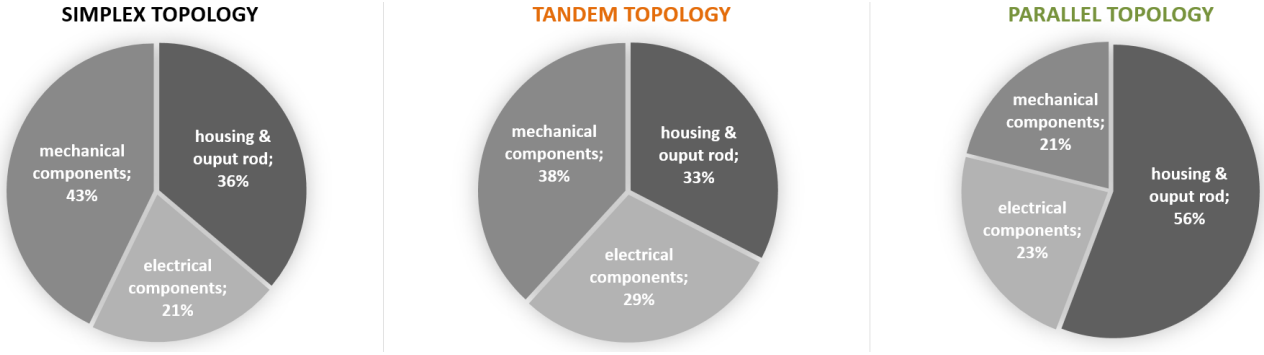


**Figure 23.** Component mass distribution for one actuator.

The parallel configuration seemed to be a relevant choice because of the load reduction. However, this finally penalizes the actuator because the load reduction involves a small actuator diameter. With the increase in the stroke, the diameter-to-length ratio is not interesting anymore. There is not any mass gain on the housing and output rod. The cross bar has to be considered in the mass statement too.

Finally, the total actuation mass gain involved by the parallel topology is not significant enough relatively to the potential drawbacks it introduces.

### *7.3. Sizing of Main and Tail Rotor Actuators*

Section 3 showed that the TRA application was distinguished from the MRA in terms of dynamism, load, and especially in terms of induced motor losses. To illustrate this difference between the MRA and TRA applications (Table 1), their specifications are executed into the sizing code. The sized motor characteristics and an actuator mass distribution are displayed in Figures 24 and 25.

Figure 25 shows the important mass decrease among components induced by the TRA application. The TRA total mass shows to be 80% smaller than the actuator, satisfying both applications.

For confidentiality reasons, the results of the MRA and TRA sizing are normalized. The reference is taken as the actuator sizing which satisfies both applications at the same time.

Figure 24 globally shows that the selected motor for the TRA has reduced characteristics compared to the one selected for the MRA. The rotor inertia, which induces motor losses, is drastically lowered compared to the MRA-selected motor.

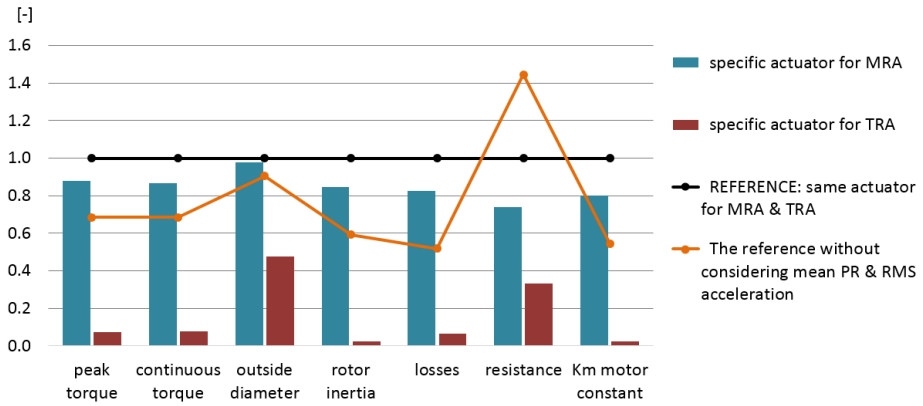


**Figure 24.** Motor characteristic evolution of specific actuators for the MRA and TRA applications compared to a unique actuator for both applications (reference).

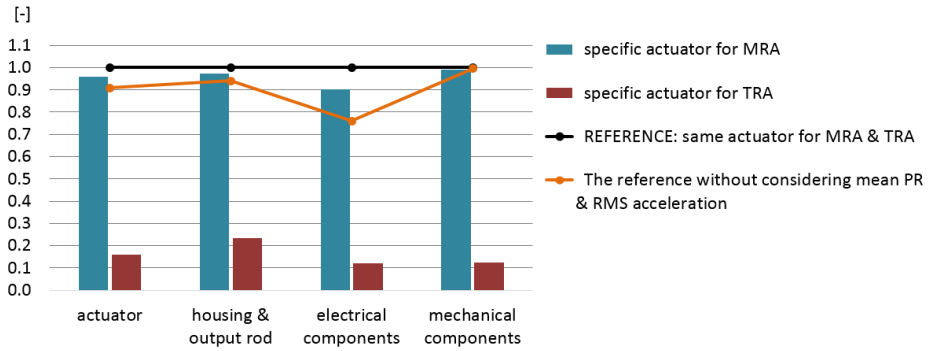


**Figure 25.** Mass distribution of specific actuators for the MRA and TRA applications compared to a unique actuator for both applications.

Section 3 suggests the mean power rate $\overline{PR}$ and the RMS acceleration $a_{rms}$ as a way to consider the induced motor losses. In Figure 24, the orange line shows the sizing resulting from the reference actuator specification regardless of $\overline{PR}$ and $a_{rms}$. The losses result to be estimated at roughly 40% of what they are for the reference actuator, and the continuous torque is at roughly 70%. The performance difference is also seen through the actuator mass statement in Figure 25. It is clear that not considering the values $\overline{PR}$ and $a_{rms}$ in the actuator specification involves a significant risk of undersizing the electrical motor of the actuator.

The MRA and TRA of the considered helicopter PFCS lead to two significantly different sizes. The MRA and TRA are two applications to be distinguished. Designing a specific actuator for each application will benefit the helicopter mass and its electrical network.

## 8. Discussion

This paper presents a design methodology supported by tools for the preliminary sizing of critical actuators. This methodology can be applied to any actuator architectures. This methodology finds an extension to the design of multirotor drones as presented in [44]. Moreover, it completes, at the component level, the methodology proposed by [45] at the vehicle level. The author of [45] developed a power system architecture sizing process for the preliminary design phase of civil aircraft.

The first tool presented is the one from [3]. It is a data-driven specification methodology which draws a parallel between measurement data on flight and EMA technologies using indicators to estimate over mission profiles.

Nowadays, the industrial context comes to a digital twin. Data content is globally exponentially increasing. As a result, there is a necessity to develop such data analysis methodologies based on synthetic values. What is more, the industrial trend is to reduce the number of helicopter flight tests to shrink development costs. Consequently, the methodology must extract as much added value as possible from any available data. The paper [3] presents a statistical approach getting interest in this area. From a reduced data set, the statistical laws are formulated. The laws are used then to express the load, speed, and acceleration domain limits of the application.

Furthermore, as seen in this paper, the specification methodology applied on main and tail rotor applications taught about the helicopter specificities. It showed a clear dynamism and load difference between the MRA and the TRA. The indicators quantified the importance of the motor losses on the TRA compared to the MRA. These losses are induced by the mean power rate $\overline{PR}$ and especially the equivalent continuous acceleration $a_{rms}$. The last part of the paper showed the risk of undersizing if $a_{rms}$ and $\overline{PR}$ are not taken into account. In addition, it concludes that the helicopter mass could benefit from a specific sizing for the MRA and the TRA. The TRA shall be designed with a rotor inertia as low as possible.

The second tool presented is the scaling laws based on a dimensional analysis. The electrical motor is chosen as an applicative example. The scaling laws capture the main physical phenomena driving the component design and easily estimate the main component

characteristics from a reduced number of parameters. As illustrated by the last part of this paper, the scaling laws are useful for the exploration study of a design domain: sizing with optimization, a scenario analysis, an integration study (mass and dimensions), and a technology or architecture comparison. In addition, scaling laws can be useful to replace component catalogs when they are unavailable or to complete missing contents. In the context of negotiation, scaling laws are easy enough to exchange with suppliers and to challenge them.

The third tool presented is a surrogate model or response surface model (RSM). It is set up using dimensionless numbers (or $\pi$-numbers). This has several advantages. First, it decreases the number of variables to be manipulated and therefore it drastically decreases the number of physical or numerical experiments to be carried out. Secondly, it increases the regression robustness [32], in particular if the RSM is built within the logarithmic space. Paper [17] mentions that the logarithmic shows good results in interpolation and in extrapolation because of the power-law form. This is the case for the VPLM methodology (Variable Power-Law Metamodel) [31] used in the surrogate model setup in this paper.

The complex vibratory problem of the actuator housing is suggested to be addressed by a surrogate model because it is adapted to preliminary studies. Indeed, it is a simple way of modeling with a reduced number of parameters. The suggested model easily provides design trends for architecture decision making. This is shown in the last part of this paper where the actuator topologies are compared. Obviously, the final actuator housing design will require laboratory experiments on a vibratory test bench.

Finally, as perspectives, the presented design methodology can be applied to any other actuator architectures. Thus, for a given application, it allows to study and select the best actuator architecture. For critical actuators, an analysis among different redundant topologies of actuation and a safety analysis with failure trees are important features to develop. In addition, a price assessment is a relevant feature to implement.

**Author Contributions:** Conceptualization, J.R., M.B. and L.R.; methodology, J.R., M.B. and L.R.; software, J.R. and M.B.; validation, J.R., M.B. and L.R.; formal analysis, J.R. and M.B.; investigation, J.R. and M.B.; resources, J.R. and M.B.; data curation, J.R. and M.B.; writing—original draft preparation, J.R.; writing—review and editing, J.R. and M.B.; visualization, J.R.; supervision, M.B. and L.R.; project administration, J.R.; funding acquisition, J.R. All authors have read and agreed to the published version of the manuscript.

**Funding:** This research was funded by Airbus Helicopters and the French Minister of Higher Education, Research and Innovation (MESRI) through the French National Association of Research and Technology (ANRT).

**Institutional Review Board Statement:** Not applicable.

**Informed Consent Statement:** Not applicable.

**Data Availability Statement:** Not applicable.

**Acknowledgments:** The authors would like to acknowledge Airbus and the ANRT who funded the PhD thesis that produced the work presented in this paper.

**Conflicts of Interest:** The authors declare no conflict of interest.

## Nomenclature

| Symbol | Unit | Name | Symbol | Unit | Name |
|---|---|---|---|---|---|
| | | Section 3 | | | |
| $a(t)$ | $m \cdot s^{-2}$ | acceleration on mission profiles | $F(t)$ | N | load on mission profiles |
| $s$ | m | stroke | $v(t)$ | $m \cdot s^{-1}$ | speed on mission profiles |
| $PR$ | $N \cdot m \cdot s^{-2}$ | power rate | $\overline{PR}$ | $N \cdot m \cdot s^{-2}$ | mean power rate |
| $a_{PRmax}$ | $m \cdot s^{-2}$ | acceleration at maximum power rate | $F_{PRmax}$ | N | load at maximum power rate |

| Symbol | Unit | Name | Symbol | Unit | Name |
|---|---|---|---|---|---|
| | | Section 5 | | | |
| $x^*$ | - | scaling ratio $x/x_{ref}$ | $\pi_i$ | - | $\pi$-number |
| $x_{ref}$ | [x] | characteristic of component of reference used in scaling law | | | |
| $d$ | m | dimension or diameter | $p$ | [p] | material property |
| $L$ | m | characteristic length | $M$ | kg | mass |
| $\rho$ | $kg \cdot m^{-3}$ | density | $V$ | $m^3$ | volume |
| $T$ | $m \cdot N$ | torque | $T_p$ | $m \cdot N$ | peak torque |
| $\alpha$ | $m^{-1} \cdot N^{-1} \cdot W$ | copper losses coefficient | $\beta$ | $rad^{-1} \cdot s \cdot W$ | iron losses coefficient |
| $f_{elect}$ | $rad \cdot s^{-1}$ | electrical speed | $\Omega$ | $rad \cdot s^{-1}$ | angular speed |
| $K_m$ | $m^2 \cdot N^2 \cdot W^{-1}$ | motor constant | $Q$ | W | heat |
| | | Section 6 | | | |
| $x$ | m | vibratory displacement amplitude | $f_r$ | hz | first resonance mode frequency |
| $a$ | $m \cdot s^{-2}$ | amplitude of sinusoidal vibratory acceleration | | | |
| $\omega$ | $rad \cdot s^{-1}$ | angular frequency | $L_a$ | m | actuator total length |
| $e_1$ | m | housing thickness | $e_2$ | m | output rod thickness |
| $d_{rs}$ | m | roller-screw nut diameter | $L_{rs}$ | m | roller-screw nut length |
| $M_{eq}$ | kg | equivalent mass | $K_{eq}$ | $N \cdot m^{-1}$ | equivalent stiffness |
| $C_{eq}$ | $N \cdot m^{-1} \cdot s$ | equivalent damping | $\xi$ | - | equivalent damping coefficient |
| $x_0$ | [x] | value of $x$ at first resonance mode | $F$ | N | excitation load applied on $M_{eq}$ |
| $U$ | m | displacement of $M_{eq}$ | $u$ | m | actuator deflection |
| $V$ | $m \cdot s^{-1}$ | speed of $M_{eq}$ | $v$ | $m \cdot s^{-1}$ | actuator deflection speed |
| $\sigma$ | Pa | actuator housing stress | $Q_m$ | - | actuator quality factor |
| $E$ | Pa | Young's modulus of actuator material | $\rho$ | $kg \cdot m^{-3}$ | density of actuator material |

## Abbreviations

The following abbreviations are used in this manuscript:

| | |
|---|---|
| BB1 | Angular Contact Double-row Ball Bearing |
| BB2 | Deep Groove Single-row Ball Bearing |
| DoE | Design of Experiment |
| DDV | Direct Drive Valve |
| EM | Electrical Motor (PMSM) |
| EMA | Electromechanical Actuator |
| EMB | Electromagnetic Brake |
| FCC | Flight Control Computer |
| FCL | Flight Control Links |
| H | Housing |
| IDF | Individual Disciplinary Feasible |
| KDD | Key Design Driver |
| MDO | Multidisciplinary Design Optimization |
| MRA | Main Rotor Actuator |
| OPV | Optionally Piloted Vehicle |
| OR | Output Rod |
| PFCS | Primary Flight Control System |
| RE | Rod End |
| RMC | Root Mean Cube |
| RMS | Root Mean Square |
| RSM | Response Surface Model |
| SFCS | Secondary Flight Control System |
| SM | Screw Mechanism |
| TRA | Tail Rotor Actuator |
| UAM | Urban Air Mobility |
| UAS | Unmanned Aerial System |
| UAV | Unmanned Aerial Vehicle |
| VPLM | Variable Power-Law Metamodel |
| VTOL | Vertical Take-off Landing |

## Appendix A. Surrogate Model: Housing of the Tandem Topology of Actuation

For the tandem topology of actuation and at the interface between output rod and housing, the regression gives the following surrogate model:

$$\begin{aligned} log_{10}(\pi_0) = {} & 180 \cdot log_{10}\left(\frac{L}{d}\right)^2 \cdot \frac{1}{983} + 23 \cdot log_{10}\left(\frac{L}{d}\right) \cdot log_{10}\left(\frac{e_1}{d}\right) \cdot \frac{1}{243} + 43 \cdot log_{10}\left(\frac{L}{d}\right) \cdot log_{10}\left(\frac{e_2}{d}\right) \cdot \frac{1}{880} \\ & + 1187 \cdot log_{10}\left(\frac{L}{d}\right) \cdot \frac{1}{766} + 149 \cdot log_{10}\left(\frac{e_1}{d}\right)^2 \cdot \frac{1}{993} + 179 \cdot log_{10}\left(\frac{e_1}{d}\right) \cdot log_{10}\left(\frac{e_2}{d}\right) \cdot \frac{1}{712} \\ & - 175 \cdot log_{10}\left(\frac{e_1}{d}\right) \cdot \frac{1}{429} + 625 \cdot log_{10}\left(\frac{e_2}{d}\right)^2 \cdot \frac{1}{791} + 1229 \cdot log_{10}\left(\frac{e_2}{d}\right) \cdot \frac{1}{694} + \frac{922}{999} \end{aligned} \tag{A1}$$

with $L$ the length $L_a$ and $d$ the diameter $d_{rs}$.

For the tandem topology of actuation and at the interface between both actuators, the regression gives the following surrogate model:

$$\begin{aligned} log_{10}(\pi_0) = {} & 96 \cdot log_{10}\left(\frac{L}{d}\right)^2 \cdot \frac{1}{899} + 25 \cdot log_{10}\left(\frac{L}{d}\right) \cdot log_{10}\left(\frac{e_1}{d}\right) \cdot \frac{1}{974} + 8 \cdot log_{10}\left(\frac{L}{d}\right) \cdot log_{10}\left(\frac{e_2}{d}\right) \cdot \frac{1}{223} \\ & + 1012 \cdot log_{10}\left(\frac{L}{d}\right) \cdot \frac{1}{585} - 8 \cdot log_{10}\left(\frac{e_1}{d}\right)^2 \cdot \frac{1}{819} - 43 \cdot log_{10}\left(\frac{e_1}{d}\right) \cdot log_{10}\left(\frac{e_2}{d}\right) \cdot \frac{1}{974} \\ & - 84 \cdot log_{10}\left(\frac{e_1}{d}\right) \cdot \frac{1}{811} + 2 \cdot log_{10}\left(\frac{e_2}{d}\right)^2 \cdot \frac{1}{15} - 259 \cdot log_{10}\left(\frac{e_2}{d}\right) \cdot \frac{1}{372} - \frac{175}{731} \end{aligned} \tag{A2}$$

with $L$ the length $L_a$ and $d$ the diameter $d_{rs}$.

## References


1. Qiao, G.; Liu, G.; Shi, Z.; Wang, Y.; Ma, S.; Lim, T.C. A review of electromechanical actuators for More/All Electric aircraft systems. *Proc. Inst. Mech. Eng. Part J. Mech. Eng. Sci.* **2018**, *232*, 4128–4151. [CrossRef]
2. Cochoy, O.; Carl, U.B.; Thielecke, F. Integration and control of electromechanical and electrohydraulic actuators in a hybrid primary flight control architecture. In Proceedings of the International Conference on Recent Advances in Aerospace Actuation Systems and Components (R3ASC), Toulouse, France, 13–15 June 2007; INSA: Toulouse, France, 2007; pp. 1–8.
3. Roussel, J.; Budinger, M.; Ruet, L. Unmanned helicopter flight control actuator specification through mission profile analysis. In *Proceedings of the IOP Conference Series: Materials Science and Engineering*; IOP Publishing: Bristol, UK, 2022, Volume 1226; p. 012100. Available online: https://iopscience.iop.org/article/10.1088/1757-899X/1226/1/012100/meta (accessed on 18 August 2022).
4. Raletz, R. *Basic Theory of the Helicopter*; CEPADUES: Toulouse, France, 2010. ISBN 9782854289374.
5. FAA. *Helicopter Flying Handbook*; US Department of Transportation, 2019. Available online: https://www.faa.gov/sites/faa.gov/files/regulations_policies/handbooks_manuals/aviation/helicopter_flying_handbook/helicopter_flying_handbook.pdf (accessed on 30 July 2022).
6. Maré, J.C. *Aerospace Actuators 2: Signal-by-Wire and Power-by-Wire*; ISTE Group: London, UK, 2017; Volume 2.
7. RTCA. *Environmental Conditions and Test Procedures for Airborne Equipment, DO-160E, EUROCAE ED-14E*; RTCA: Washington, DC, USA, 2005.
8. Mazzoleni, M.; Di Rito, G.; Previdi, F. *Electro-Mechanical Actuators for the More Electric Aircraft*; Springer: Berlin/Heidelberg, Germany, 2021.
9. Liscouët, J.; Maré, J.C.; Budinger, M. An integrated methodology for the preliminary design of highly reliable electromechanical actuators: Search for architecture solutions. *Aerosp. Sci. Technol.* **2012**, *22*, 9–18. Available online: https://scholar.google.fr/citations?view_op=view_citation&hl=fr&user=nkGEGZgAAAAJ&citation_for_view=nkGEGZgAAAAJ:ufrVoPGSRksC (accessed on 30 July 2022). [CrossRef]
10. Andersson, J.; Krus, P.; Nilsson, K. Optimization as a support for selection and design of aircraft actuation systems. In Proceedings of the 7th AIAA/USAF/NASA/ISSMO Symposium on Multidisciplinary Analysis and Optimization, St. Louis, MO, USA, 2–4 September 1998; p. 4887.
11. Jiao, Z.; Yu, B.; Wu, S.; Shang, Y.; Huang, H.; Tang, Z.; Wei, R.; Li, C. An intelligent design method for actuation system architecture optimization for more electrical aircraft. *Aerosp. Sci. Technol.* **2019**, *93*, 105079. [CrossRef]
12. Roos, F. On Design Methods for Mechatronics: Servo Motor and Gearhead. Ph.D. Thesis, Royal Institute of Technology, Stockholm, Sweden, 2005.

13. Roos, F.; Johansson, H.; Wikander, J. Optimal selection of motor and gearhead in mechatronic applications. *Mechatronics* **2006**, *16*, 63–72. [CrossRef]
14. Pfennig, M.; Carl, U.B.; Thielecke, F. Recent advances towards an integrated and optimized design of high lift actuation systems. *SAE Int.l J. Aerosp.* **2010**, *3*, 55. [CrossRef]
15. Wu, S.; Yu, B.; Jiao, Z.; Shang, Y.; Luk, P. Preliminary design and multi-objective optimization of electro-hydrostatic actuator. *Proc. Inst. Mech. Eng. Part J. Aerosp. Eng.* **2017**, *231*, 1258–1268. [CrossRef]
16. Raymer, D. *Aircraft Design: A Conceptual Approach*; American Institute of Aeronautics and Astronautics, Inc.: Reston, VA, USA, 2012.
17. Budinger, M.; Reysset, A.; Ochotorena, A.; Delbecq, S. Scaling laws and similarity models for the preliminary design of multirotor drones. *Aerosp. Sci. Technol.* **2020**, *98*, 105658. [CrossRef]
18. Massachusetts, I.o.T. Thermodynamic and Propulsion—Aircraft Engine Performance— Performance of Propellers. Online MIT Resource. 2022. Available online: https://web.mit.edu/16.unified/www/FALL/thermodynamics/notes/node86.html (accessed on 30 July 2022).
19. McCormick, B.W.; Aljabri, A.S.; Jumper, S.J.; Martinovic, Z.N. The Analysis of Propellers Including Interaction Effects. *NASA Scientific and Technical Information Facility*. 1979. Available online: https://www.researchgate.net/publication/23913137_The_Analysis_of_Propellers_Including_Interaction_Effects:2022/07 (accessed on 30 July 2022).
20. Saerens, E.; Crispel, S.; Garcia, P.L.; Verstraten, T.; Ducastel, V.; Vanderborght, B.; Lefeber, D. Scaling laws for robotic transmissions. *Mech. Mach. Theory* **2019**, *140*, 601–621. [CrossRef]
21. Papalambros, P.Y.; Wilde, D.J. *Principles of Optimal Design: Modeling and Computation*, 2nd ed.; Cambridge University Press: Cambridge, UK; New York, NY, USA, 2000.
22. Martins, J.R.; Lambe, A.B. Multidisciplinary design optimization: A survey of architectures. *AIAA J.* **2013**, *51*, 2049–2075. [CrossRef]
23. Budinger, M.; Reysset, A.; Halabi, T.E.; Vasiliu, C.; Maré, J.C. Optimal preliminary design of electromechanical actuators. *Proc. Inst. Mech. Eng. Part G J. Aerosp. Eng.* **2014**, *228*, 1598–1616. [CrossRef]
24. Reysset, A.; Budinger, M.; Maré, J.C. Computer-aided definition of sizing procedures and optimization problems of mechatronic systems. *Concurr. Eng.* **2015**, *23*, 320–332. [CrossRef]
25. Delbecq, S.; Budinger, M.; Reysset, A. Benchmarking of monolithic MDO formulations and derivative computation techniques using OpenMDAO. *Struct. Multidiscip. Optim.* **2020**, *62*, 645–666. [CrossRef]
26. Jaafar, A. Analysis of Mission Profiles and Environment Variables for Integration into the Systemic Design Processus. Ph.D. Thesis, INP, Toulouse, France, 2011.
27. Reysset, A. Preliminary Design of Electromechanical Actuators—Tools to Support the Specification and the Generation of Sizing Procedures for the Optimization. Ph.D. Thesis, INSA, Toulouse, France, 2015.
28. Hehenberger, P.; Poltschak, F.; Zeman, K.; Amrhein, W. Hierarchical design models in the mechatronic product development process of synchronous machines. *Mechatronics* **2010**, *20*, 864–875. [CrossRef]
29. Van Groesen, E.; Molenaar, J. *Continuum Modeling in the Physical Sciences*; SIAM: Bangkok, Thailand, 2007. Volume 13; pp. 1–29.
30. Holmes, M.H. Dimensional Analysis (chapter). In *Introduction to the Foundations of Applied Mathematics*; Springer: Berlin/Heidelberg, Germany, 2019; pp. 1–47.
31. Sanchez, F.; Budinger, M.; Hazyuk, I. Dimensional analysis and surrogate models for the thermal modeling of Multiphysics systems. *Appl. Therm. Eng.* **2017**, *110*, 758–771. [CrossRef]
32. Lacey, D.; Steele, C. The use of dimensional analysis to augment design of experiments for optimization and robustification. *J. Eng. Des.* **2006**, *17*, 55–73. [CrossRef]
33. Budinger, M.; Liscouët, J.; Hospital, F.; Maré, J. Estimation models for the preliminary design of electromechanical actuators. *Proc. Inst. Mech. Eng. Part J. Aerosp. Eng.* **2012**, *226*, 243–259. [CrossRef]
34. Jufer, M. Design and losses-scaling law approach. In Proceedings of the Nordic Research Symposium Energy Efficient Electric Motors and Drives, Skagen, Denmark, January, 1996; pp. 21–25. Available online: https://www.researchgate.net/profile/Marcel-Jufer/publication/288811698_Design_and_Losses-Scaling_Law_Approach/links/6146d76e3c6cb310697a4154/Design-and-Losses-Scaling-Law-Approach.pdf (accessed on 18 August 2022).
35. PARKER. Frameless Low Cogging Servo Motors—NK Series. 2022. Available online: https://ph.parker.com/us/en/frameless-low-cogging-servo-motors-nk-series/nk630esrr1000 (accessed on 30 July 2022).
36. KOLLMORGEN. RBE Series Brushless Motors for Frameless DDR (Direct Drive Rotary) Motor Applications, 2003. Available online: http://www.kollmorgen.com/ (accessed on 30 July 2022).
37. Grellet, G. *TI Technics of the Engineer—d3450v1—Losses in the Spinning Machines*; Technics of the Engineer Editions: Saint-Denis, France, 1989.
38. Budinger, M.; Reysset, A.; Maré, J.C. Preliminary design of aerospace linear actuator housings. *Aircr. Eng. Aerosp. Technol. Int. J.* **2015**, *87*, 224–237.
39. EASA. *Certification Specifications and Acceptable Means of Compliance for Large Aeroplanes CS-25 Amendment 4*; EASA: Cologne, Germany, 2007.
40. Nicolas, M. Continuum and Discrete Mechanics. Available online: https://cel.archives-ouvertes.fr/cel-00612360v1/document. (accessed on 30 July 2022).

41. Spencer, A.J.M. *Continuum Mechanics*; Courier Corporation, North Chelmsford, MA, USA, 2004; ISBN 978-0486435947.
42. Naubert, A.; Bachmann, M.; Binz, H.; Christmann, M.; Perni, F.; Toro, S. Disconnect device design options for jam-tolerant EMAs. In Proceedings of the International Conference on Recent Advances in Aerospace Actuation Systems and Components (R3ASC), Toulouse, France, 16–17 March 2016; INSA Toulouse: Toulouse, France, 2016; pp. 187–192.
43. Seemann, S.; Christmann, M.; Jänker, P.J. Control and monitoring concept for a fault-tolerant electromechanical actuation system, EADS Innovation Work. In Proceedings of the International Conference on Recent Advances in Aerospace Actuation Systems and Components (R3ASC), Toulouse, France, 13–14 June 2012; INSA Toulouse: Toulouse, France, 2012; pp. 39–43.
44. Delbecq, S.; Budinger, M.; Ochotorena, A.; Reysset, A.; Defaÿ, F. Efficient sizing and optimization of multirotor drones based on scaling laws and similarity models. *Aerosp. Sci. Technol.* **2020**, *102*, 105873. [CrossRef]
45. Liscouet-Hanke, S. A Model-Based Methodology for Integrated Preliminary Sizing and Analysis of Aircraft Power System Architectures. Ph.D. Thesis, Institut National des Sciences Appliquées de Toulouse, Toulouse, France, 2008.